AGU ADVANCING EARTH AND SPACE SCIENCES

Space Weather

RESEARCH ARTICLE
10.1029/2024SW004307

Dynamics of TEC High Density Regions Seen in JPL GIMs: Variations With Latitude, Season and Geomagnetic Activity

M. A. Cafolla[1], S. C. Chapman[1], N. W. Watkins[1,2], X. Meng[3], and O. P. Verkhoglyadova[3]

[1]Physics Department, Centre for Fusion, Space and Astrophysics, Physics Department, University of Warwick, Coventry, UK, [2]London School of Economics and Political Science, Grantham Research Institute on Climate Change and the Environment, London, UK, [3]Jet Propulsion Laboratory, California Institute of Technology, Pasadena, CA, USA

Key Points:

- High Density Regions of Total Electron Content identified as space-time objects in 20 years of 15 min global maps using a quantile threshold
- High Density Regions (HDRs) form two distinct populations that are smaller than, or are of order, continental scale in peak area
- HDRs form at four magnetic latitude bands regardless of season, geomagnetic activity level. Significant subset track constant magnetic latitude

Correspondence to:

M. A. Cafolla,
martin.cafolla.1@warwick.ac.uk

Citation:

Cafolla, M. A., Chapman, S. C., Watkins, N. W., Meng, X., & Verkhoglyadova, O. P. (2025). Dynamics of TEC high density regions seen in JPL GIMs: Variations with latitude, season and geomagnetic activity. *Space Weather*, *23*, e2024SW004307. https://doi.org/10.1029/2024SW004307

Received 10 DEC 2024
Accepted 10 MAR 2025

Author Contributions:

Conceptualization: M. A. Cafolla, S. C. Chapman
Data curation: X. Meng, O. P. Verkhoglyadova
Formal analysis: M. A. Cafolla, S. C. Chapman
Funding acquisition: S. C. Chapman, O. P. Verkhoglyadova
Investigation: M. A. Cafolla, S. C. Chapman
Methodology: M. A. Cafolla, S. C. Chapman
Project administration: S. C. Chapman
Resources: S. C. Chapman, X. Meng, O. P. Verkhoglyadova
Software: M. A. Cafolla
Supervision: S. C. Chapman, N. W. Watkins
Validation: M. A. Cafolla, S. C. Chapman, N. W. Watkins, X. Meng, O. P. Verkhoglyadova
Visualization: M. A. Cafolla

Abstract

Total Electron Content (TEC) is central to characterizing ionospheric response to solar and geomagnetic activity. Variations in TEC structures over time provide insight into underlying physical processes and inform monitoring of space weather events, which pose a risk to navigation and communication systems. JPL processed GNSS observations over 20 years provide a series of 15-min Global Ionospheric Maps (GIMs) of spatial resolution $1^\circ \times 1^\circ$ longitude/latitude. We translate these into geomagnetic coordinates centered about the sub-solar point and we isolate the top 1% of TEC values in each map to define High Density Regions (HDRs) of TEC. Image processing tools are used to develop an algorithm that detects and tracks these to compile a set of contiguous, uniquely labeled space-time TEC HDRs. We find that HDRs naturally divide into two populations by peak area, separated by a size of $8.0 \times 10^6 \text{km}^2$, which is around the continental scale. These populations are studied for different storm conditions—quiet ($\text{Kp} < 4$), moderate ($4 \leq \text{Kp} < 7$) and extreme ($\text{Kp} \geq 7$): small HDRs form primarily around four magnetic latitude bands and move roughly parallel to lines of constant magnetic latitude toward later MLT. Large HDRs form around the same latitude bands but follow more complex paths. The statistical nature of these results could be used in predictive ionospheric models and identify reproducible trends on these spatial/temporal scales.

Plain Language Summary

The ionosphere is a layer above the atmosphere consisting of free electrons and ions. Due to differing levels of exposure to solar radiation, cosmic rays and the effect of geomagnetic activity, the number density of electrons varies across the ionosphere. This will result in regions of high and low electron number densities of varying shapes, sizes, and lifetime. We first define a method to find High Density Regions (HDRs), that is areas of enhanced line-integrated electron number density, using a quantile TEC threshold. We then develop an algorithm that identifies, isolates then tracks these regions for 20 years of TEC data. From this new data set of contiguous space-time enhancements we conduct a statistical study to look for noticeable trends in HDR location, size, trajectory and duration. Our results provide an insight into future HDR behavior; in particular, given geomagnetic indices we can begin to predict the location and path over which space weather events may cause the largest enhancements of TEC, thus identifying regions that are most likely to experience problems with communication/navigation under specific geomagnetic conditions.

1. Introduction

Ionospheric structures can be characterized by Total Electron Content (TEC), the height-integrated electron column density along a line-of-sight path between satellites and ground receivers (Janssen, 2012; Lalgudi Gopalakrishnan & Schmidt, 2022). This electron density varies with altitude, with the highest concentration of TEC found between $\sim 350 - 500$km (Bilitza et al., 2022; Hernández-Pajares et al., 2011; Immel et al., 2006; Keskinen et al., 2003; Lalgudi Gopalakrishnan & Schmidt, 2022; Wang et al., 2016). The Global Navigation Satellite System (GNSS) has facilitated the measurement of TEC globally, across a range of scales captured by 2D or 3D ionospheric maps. Previous work includes regional analysis over countries/continents (Badeke et al., 2018; Z. Chen et al., 2015; Doherty et al., 2004; Kintner & Lledvina, 2004; J. Y. Liu et al., 2013; Seemala & Valladares, 2011; Takahashi et al., 2016) up to global coverage (Astafyeva et al., 2008; P. Chen et al., 2022; Emmert et al., 2017; He et al., 2024; Janssen, 2012; L. Liu et al., 2009; Mannucci et al., 1998; Martire et al., 2024; Meng et al., 2024; Nikitina et al., 2022; Tsai et al., 2019; Verkhoglyadova et al., 2021). The TEC database is accumulated over the last couple of solar cycles, in which it is possible to see patterns in TEC spatial-temporal variation across the globe over hourly, Earth/solar rotation, seasonal and yearly scales as well as sensitivity to geomagnetic activity (Amiri-Simkooei & Asgari, 2012; Aravindan & Iyer, 1990; Badeke et al., 2018; Buzulukova

Writing – original draft: M. A. Cafolla
Writing – review & editing: M. A. Cafolla, S. C. Chapman, N. W. Watkins, X. Meng, O. P. Verkhoglyadova

& Tsurutani, 2022; Knudsen, 2022; Nikitina et al., 2022; Qian et al., 2013; Yasyukevich & Yasyukevich, 2021). Identifying the occurrence likelihood of rapidly changing TEC enhancements, along with regions at which these enhancements are most likely, is important to space weather monitoring/risk identification, since large-scale TEC fluctuations can result in major perturbations to radio communication and navigation signals propagating through the ionosphere (Alcay & Gungor, 2020; Janssen, 2012; Pulkkinen, 2007).

A common feature seen in the low-latitude ionosphere is the Equatorial Ionization Anomaly (EIA). In general this is a two-peak TEC intensification located at magnetic latitudes of $\sim\pm 10 - 20°$ (Balan, Souza, & Bailey, 2018; Balan, Liu, & Le, 2018; Cai et al., 2022; Wood et al., 2022). From extensive analysis of EIAs over the last few decades, it is well understood that their formation mechanism involves vertical $\mathbf{E} \times \mathbf{B}$ drifts that move plasma along field lines known as the Fountain Effect (Y. Chen et al., 2016; P. Chen et al., 2022; Dunn et al., 2024; He et al., 2024; Luan, 2021; Nigussie et al., 2022; Oryema et al., 2015; Sparks et al., 2021; Walker, 1981). Not all EIAs exhibit a dual-peak structure however; a significant number of EIAs observed are single-crest TEC enhancements, primarily in the northern hemisphere (Fathy & Ghamry, 2017; L. Huang et al., 2014; Meng et al., 2024). Three, four or even more enhancements have also been detected (Cai et al., 2022; Y. Huang et al., 2024; Maruyama et al., 2016; Tsai et al., 2019; Tulasi Ram et al., 2009). The mechanisms for the formation of single/extra peaks are not as well understood. Under quiet geomagnetic conditions it has been suggested that extra peaks arise due to a combination of drivers, for example, $\mathbf{E} \times \mathbf{B}$ drifts over a range of latitudes (Cai et al., 2022; Maruyama et al., 2016; Tsai et al., 2019), neutral winds as a result of coupling with the thermosphere (Balan, Liu, & Le, 2018; Balan, Souza, & Bailey, 2018; Immel et al., 2006; Lin et al., 2005) and plasma bubbles from the nightside ionosphere (McClure et al., 1977; Patil et al., 2023). For active geomagnetic conditions it is possible that these peaks could be influenced by Storm Enhanced Densities, large-scale ionospheric electron density enhancements found in the afternoon ionosphere at mid-latitudes (Foster, 1993; J. Liu et al., 2016).

Global Ionospheric Maps (GIMs) provide continuous spatial observations of ionospheric structures over a range of temporal scales. Different types of global maps have been used to investigate ionospheric structures, for example, gridded TEC maps produced from GNSS ground-based measurements (Li et al., 2019; Mannucci et al., 1998) and climatological maps using radio occultation measurements between satellites (Anthes, 2011; Tulasi Ram et al., 2009; Yue et al., 2015). Recently, image processing techniques driven by machine learning have been applied to ionospheric TEC maps (both globally and locally) to identify trends and patterns seen in large-scale TEC enhancements and structures (Adkins & England, 2023; Rukundo et al., 2023; Verkhoglyadova et al., 2022). Meng et al. (2024) considered the statistical characteristics of the number of TEC intensifications and their resulting enhancements in global TEC maps produced by the Jet Propulsion Laboratory (JPL) using 20 years of data between 2003 − 2022. They showed that most maps follow the classic two-peak EIA structure as outlined previously, with the strength of these enhancements varying with geomagnetic activity independent of the number detected.

This paper focuses on the dynamics of these regions of enhanced TEC, in particular we aim to determine where these enhancements form and their subsequent motion for given initial conditions. We work in geomagnetic, sun-centered coordinates, described in Section 2, as TEC variations can be driven by geomagnetic activity. A quantile threshold is used to isolate High Density Regions (HDRs) of TEC, that is, areas of enhanced line-integrated electron number density. This procedure is described in Section 3. We then apply image processing tools to detect and track these regions in an automated manner in Section 4. This is done for 20 years of TEC maps from 2003 − 2022 to generate a data set of fully labeled, contiguous large-scale space-time TEC enhancements with information about their location, path, duration, size and intensity. We analyse the response of these properties to season, geomagnetic activity and geomagnetic latitude in Section 5. Our results identify features of ionospheric enhancements that are reproducible in a statistical sense. This in turn offers an ensemble level constraint for ionospheric models at given spatial/temporal resolutions, facilitating our understanding of the risks of space weather.

2. JPL Global Ionospheric Map Data in Geomagnetic Coordinates

2.1. Geographic TEC Maps Data

Global Ionospheric Maps (GIMs) provide global maps of TEC derived from GNSS data collected by ground-based receivers across the world. The maps used for this study are generated by JPL, for which there are various spatial and temporal resolutions available (Emmert et al., 2017; Mannucci et al., 1998, 1999; Martire et al., 2024; Meng & Verkhoglyadova, 2023; Verkhoglyadova et al., 2021). We use the more recent JPLD product

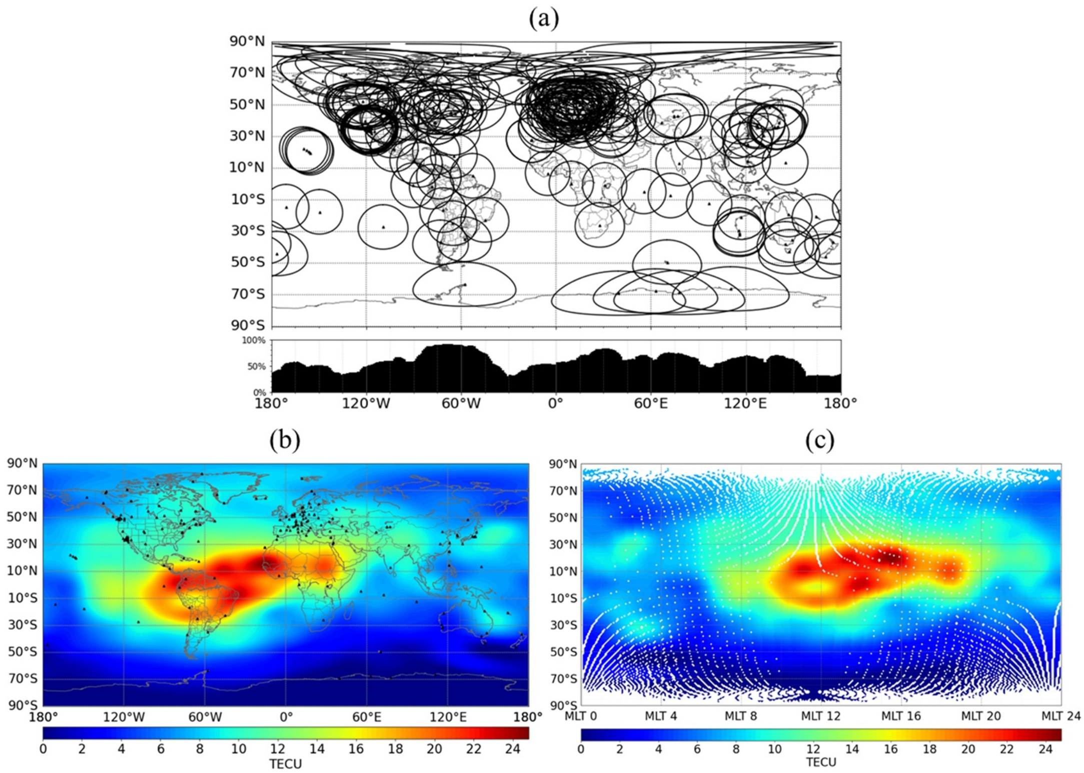

Figure 1. Example TEC map for 2009 − 07 − 23 at 16 : 30 : 00 UTC in geographic coordinates. Panel (a) plots ground stations that provide the data compiled on this date, black lines plot great circles at 10° inclination to indicate the coverage of each station. A histogram of the percentage of grid points at every 1° of longitude enclosed by these great circles is plotted across the bottom of panel (a). Panel (b) plots the resulting geographic TEC map for this date-time. Each 1° × 1° grid point plots the VTEC at that longitude/latitude. Black triangles show the locations of ground stations in both sub-figures. Panel (c) plots the same TEC map in Solar Magnetic (SM) coordinates (geomagnetic latitude vs. MLT). White grid points in the map are regions of undefined TEC resulting from the coordinate transform. The TEC values are indicated by the color-bar at the bottom of each TEC map.

(see Data Sources), taking data from 2003 to 2022 at spatial resolution 1° geographic longitude by 1° geographic latitude and temporal resolution 15 min. The number of GNSS ground-based stations varies over this time-frame, with >200 ground stations before 2018 and >300 ground stations thereafter (Meng & Verkhoglyadova, 2023). Figure 1a plots the ground stations used and the possible global coverage on 2009 − 07 − 23 using the JPL product, plotting great circles around each ground station assuming an elevation angle cut-off of 10°. The distribution of these ground stations is non-uniform, with a larger proportion of stations located in the northern hemisphere (most coverage is over Europe and the continental US). Regions with little to no coverage tend to be over the oceans. Measurements of the line of sight between ground station and satellite are read as Slant TEC (STEC) by ground stations, then re-parameterized to Vertical TEC (VTEC) for use in maps (Janssen, 2012; Lupsic & Takacs, 2022; Mannucci et al., 1998). This assumes a thin-shell ionosphere, where VTEC measurements are derived at an Ionospheric Pierce Point (IPP) at $h_{\text{iono}} = 450$km altitude (Mannucci et al., 1998; Martire et al., 2024). Gaps in the observation field are filled using interpolation from existing neighboring grids (Mannucci et al., 1998; Mendillo et al., 2005). Figure 1b plots the corresponding global TEC map for 2009 − 07 − 23 at 16 : 30 : 00 UTC (Coordinated Universal Time).

A limitation of GIMs is the non-uniform spatial sampling of regions around the world and of available signal paths between emitter and receiver. This results in undefined TEC regions which need to be filled to complete the global map. Depending on the product, there are different methods of TEC estimation including interpolation using bilinear/kriging methods (Astafyeva et al., 2008; Mannucci et al., 1998; Tsai et al., 2019) and extrapolating TEC by fitting approximations of coefficients of Spherical Harmonics (Li et al., 2019; J. Liu et al., 2011; Xiong et al., 2022; Zhang & Zhao, 2019). These estimations may lack reproducibility during strong geomagnetic activity, for example, Jehle et al. (2006) showed that difference maps between observed and modeled data gave the

10.1029/2024SW004307

largest differences during solar maximum (2003). Roma-Dollase et al. (2018) tested the consistency of TEC measurements from seven different GIM techniques over a solar cycle by comparing the vertical TEC (VTEC) approximations from these maps with millions of VTEC-altimeter measurements over various locations with differing ground-station coverage and found the largest deviations between products were during periods of strong geomagnetic activity.

2.2. Geographic to Geomagnetic TEC Coordinate Transform

We wish to analyse the dynamics of TEC enhancements ordered by the Earth's magnetic field and the position at which the Sun is directly overhead (the sub-solar point). The TEC maps are translated into Solar Magnetic (SM) coordinates, described in Appendix A1: For each geographic longitude and latitude $(\lambda_{\text{geo}}, \varphi_{\text{geo}})$ grid point from a map such as Figure 1b we find the equivalent magnetic coordinates $(\lambda_{\text{SM}}, \varphi_{\text{SM}})$ such that for each $1^\circ \times 1^\circ$ grid:

$$\text{TEC}_{\text{geo}}(\lambda_{\text{geo}}, \varphi_{\text{geo}}) \rightarrow \text{TEC}_{\text{SM}}(\lambda_{\text{SM}}(\lambda_{\text{geo}}, \varphi_{\text{geo}}), \varphi_{\text{SM}}(\lambda_{\text{geo}}, \varphi_{\text{geo}})) \tag{1}$$

This is shown in Figure 1c, with magnetic longitude defined in terms of Magnetic Local Time (MLT). By the nature of the coordinate transform, some grid points in the SM maps will contain multiple TEC values and some will be empty. For the former we assign an average TEC value to that grid point. The latter are shown as white grid points in Figure 1c and we can see that empty regions predominate nearer the poles (beyond latitudes of $\pm 70^\circ$) (Laundal & Richmond, 2017). We therefore focus our analysis on features seen within magnetic latitudes of $\pm 50^\circ$. The choice in geomagnetic coordinates for this study is such that the motion of TEC enhancements are defined relative to the sun, situated at MLT 12 at all times, and the dipole axis of the Earth's magnetic field (see Appendix A1). A straight-line trajectory with constant magnetic latitude corresponds to an ionospheric enhancement which is co-located with a fixed magnetic field line footprint in a magnetic dipole which is rotating with the Earth. Importantly, this will not be a straight-line trajectory in geographic coordinates. These dynamics of TEC enhancements are studied in Section 5. The conversion is carried out using SpacePy (see Data Sources and Nieohof et al. (2022)), which uses the International Radiation Belt Environment Modeling (IRBEM) library.

3. Fixed Quantile as an HDR Identifier

In this section we outline the procedure for identifying large-scale TEC enhancements. We define High Density Regions (HDRs) of TEC as areas with TEC values that exceed a certain threshold. Previous work used feature extraction tools such as the Laplacian operator (e.g., Verkhoglyadova et al. (2021) and Meng et al. (2024)) or applied a specific TEC value (e.g., Nikitina et al. (2022)) to define thresholds. For this study we apply a fixed quantile of the TEC data in each map as the threshold, where the q^{th} quantile of a data set is the value that exceeds $p\%$ of the data ($q = p/100$). The threshold that identifies the HDRs in each map is at a fixed quantile rather than a fixed TEC value as this ensures that each map contains at least one HDR independent of geomagnetic activity; Figure 2a shows Cumulative Density Functions (CDFs) for a subset of maps during solar cycle 24 (between 2009 and 2020) at the same timestamp of $12:00:00$ UTC. Each line is color-coded by the monthly mean sunspot number for the day in which the map is acquired to show the effect of solar cycle variations over all activity (Pulkkinen, 2007; Vaishnav et al., 2019). As expected, maps that correspond to times with a higher sunspot number have larger TEC values corresponding to a given quantile. This is further shown in Figure 2b, which selects quantiles $q = 0.99, 0.9, 0.75$ and 0.5 for the same subset of maps and plots the monthly mean sunspot number against TEC. Regardless of choice in q we find that the TEC threshold associated with that solar activity level is clustered around a linear dependence on sunspot number. The gradient between sunspot number and TEC decreases with increasing q, meaning a greater range of TEC values is seen at higher quantiles. Figure 2c plots the percentage of TEC maps between the calendar years 2003 and 2022 which have a maximum TEC value that exceeds a given TEC threshold. These figures demonstrate that using a fixed TEC threshold value would bias the identification of HDRs to maps acquired during solar maximum years. This will result in a reduced sample size of the possible 701184 maps - the percentage of available maps drops to below 50% when fixing a TEC threshold between $40 - 50$TECU.

We have shown that any choice in quantile yields a linear relationship between the sunspot number and the TEC value at quantile q. This can be used to select a specific quantile for analysis; we are interested in the behavior of extreme TEC enhancements and how these change between activity and season. Appendix B provides an example

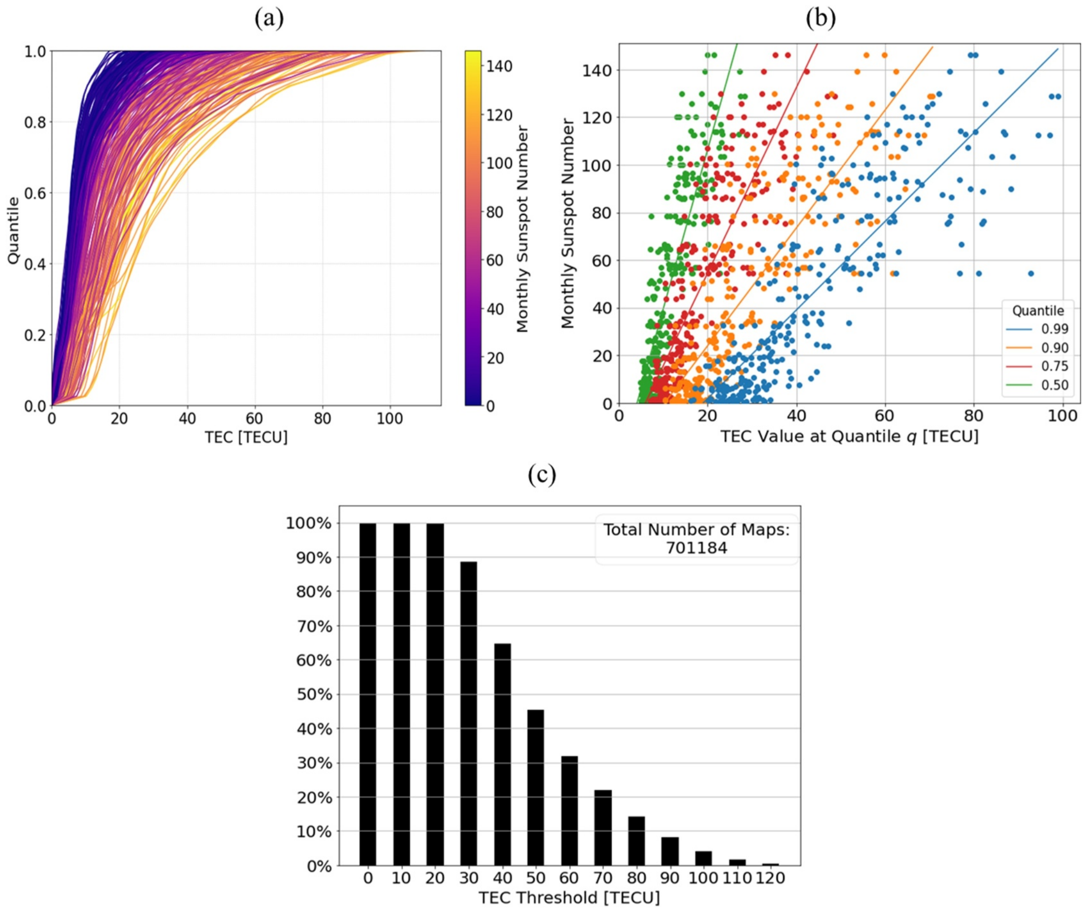

Figure 2. Panel (a) plots the CDFs of a subset of maps from solar cycle 24 (between 2009 and 2020) at $12:00:00$ UTC. Each line is color-coded to indicate the monthly mean sunspot number for that date-time. Panel (b) plots the monthly mean sunspot number for the same subset of maps against the associated TEC value for the given quantiles $q = 0.99, 0.9, 0.75$ and 0.5, defined in the legend. A straight line is fitted to each quantile data group. Panel (c) plots the percentage of maps which have a maximum TEC value that exceeds a given TEC threshold, obtained for 20 years of 15 min maps.

of HDRs at different quantiles. We define an HDR for this study as the region within which all TEC values exceed the $q = 0.99$ quantile (the top 1% of TEC). As we increase the quantile value the number of HDRs obtained will decrease. We will study the HDRs at different levels of geomagnetic activity, and the most active days will be a smaller fraction of the total data set. For the TEC maps under study we find that for Kp ≥ 7 the entire data set yields 339 for $q = 0.99$ and 236 for $q = 0.999$. On the other hand, as we decrease the quantile value we lose spatial definition of the HDRs as can be seen in the examples shown in Appendix B. We have found that the 0.99 quantile offers a good trade-off between feature identification and meaningful statistics.

We now explore how a fixed high quantile of the TEC maps tracks TEC climate over our 20 years data set. Figure 3a plots the time series of the 0.99 quantile value of TEC for two calendar years around solar maximum (2003 and 2014) and two calendar years around solar minimum (2009 and 2020), defined with respect to how F10.7 varies over the solar cycle (Meng et al., 2024; Vaishnav et al., 2019; Yaya et al., 2017). At this temporal scale we note seasonal fluctuations, where TEC values for spring and autumn are larger than for summer and winter for all years. This is consistent with enhanced geomagnetic activity driven by the Russell-McPherron effect (Russell & McPherron, 1973). Figure 3b plots the Welch estimated power spectral density for 3-year long time series spanning the calendar years $2003-2005$, $2008-2010$, $2013-2015$ and $2018-2020$ (see Python Packages section for documentation (Virtanen et al., 2020; Welch, 1967)). The spectra show peaks around frequencies corresponding to 27-day, 24-hr, 12-hr and higher frequency fluctuations as expected (Amiri-Simkooei & Asgari, 2012; Nikitina et al., 2022). We see spectra of approximately power law form for high frequencies, which flatten at periods below 12-hr. During solar maximum, all quantile values are larger than during solar minimum.

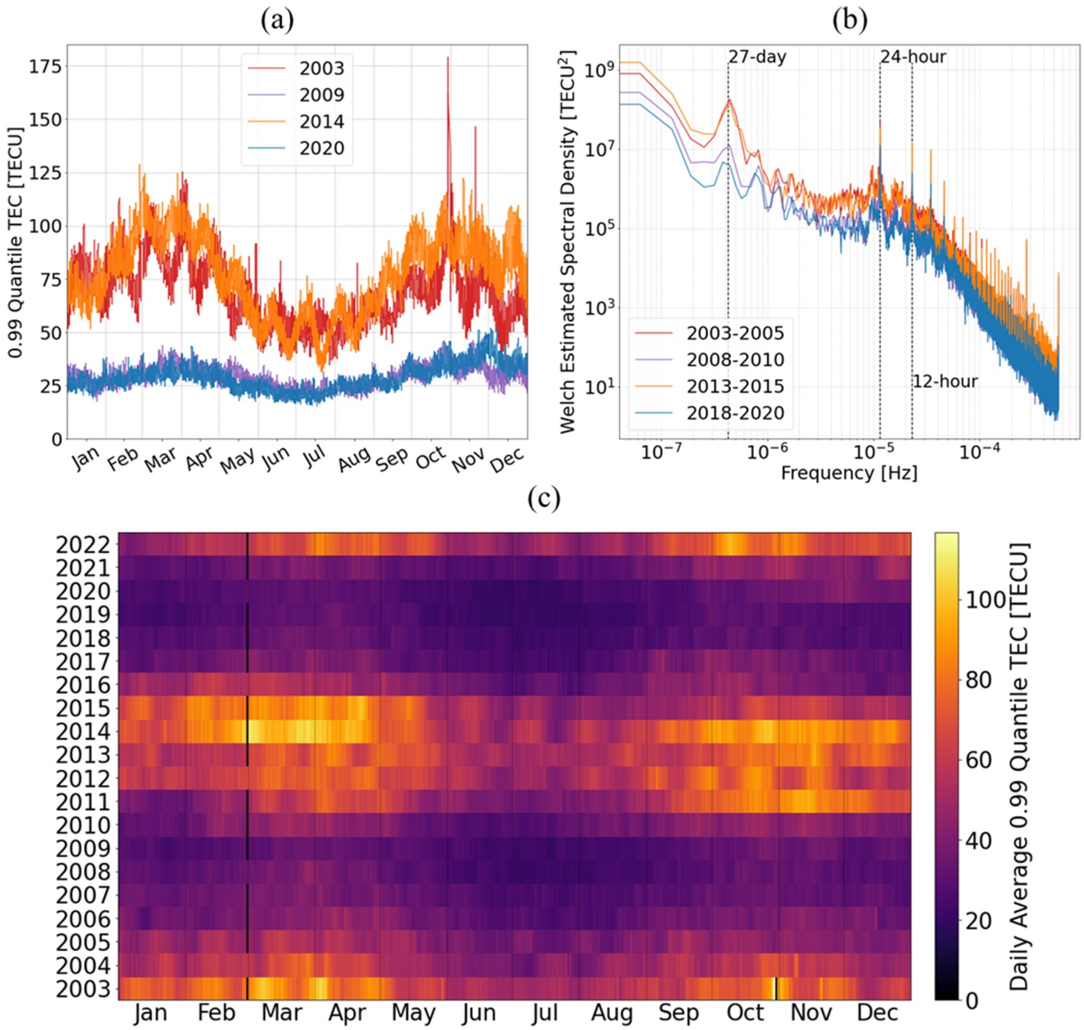

Figure 3. TEC climate as seen in the long-term variation of the 0.99 quantile of TEC. Panel (a) plots year-long time-series for 2 years during solar maximum (2003 and 2014) and 2 years during solar minimum (2009 and 2020). Panel (b) plots the Welch-estimated power spectrum for 3-year long intervals during solar maximum (2003 − 2005 and 2013 − 2015) and solar minimum (2008 − 2010 and 2018 − 2020). Vertical black dashed lines indicate frequencies at 12-hr, 24-hr, and 27 days. Panel (c) plots the daily averaged 0.99 quantile TEC on a year versus month grid. Black grid points indicate no data for that day, or alignment with leap days.

Figure 3c combines year-long time series from 1st January to 31st December for all 20 years of data into a color-mesh plot, with year along the y-axis and month along the x-axis. Each grid point plots the daily averaged value of TEC at the 0.99 quantile. Grid points along the x-axis show an approximately 27-day periodicity and along the y-axis an approximately 11-year periodicity, where the largest daily averaged TEC quantile occurs during solar maximum years (2003 and 2014). This variability tracks that of sunspot number/F10.7 over the solar cycle (Meng et al., 2024; Vaishnav et al., 2019; Yaya et al., 2017).

4. Method of HDR Detection, Tracking, and Ordering

In order to capture the dynamics of TEC enhancements we first can identify where the top 1% of TEC values lie in each map. We then can follow these enhancements in space and time in order to track their motion. In this section we present our method to isolate, detect and track HDRs and assign labels to each unique HDR using tools from the OpenCV library in Python (documentation is available in Python Packages section and Bradski (2000)). This procedure (which identifies the time varying area, the duration and the trajectories of the centroid of each HDR) is shown in Figure 4.

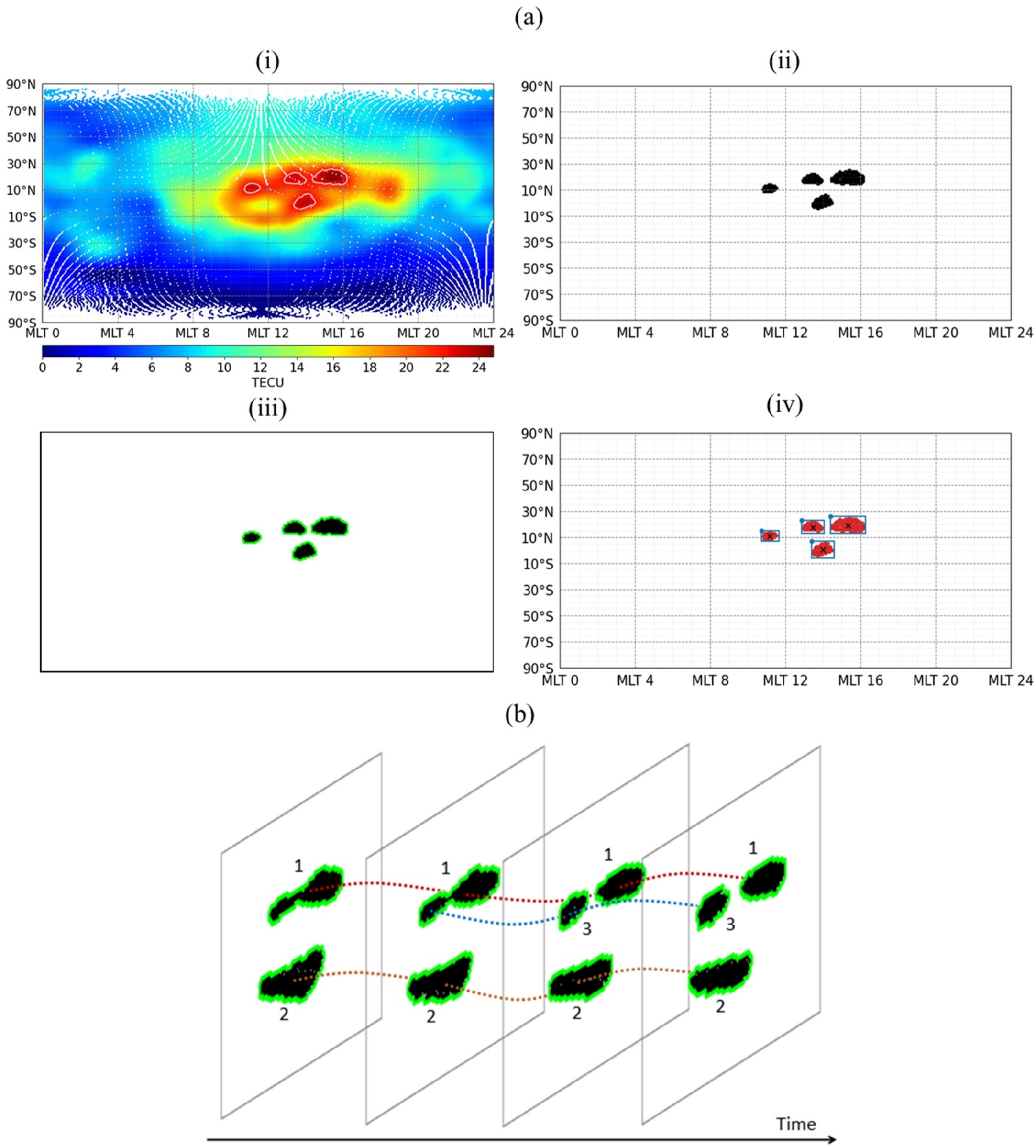

Figure 4. Sub-figure (a) outlines the procedure for HDR identification and tracking shown for TEC maps for 2009 − 07 − 23 at 16 : 30 : 00 UTC in geomagnetic coordinates. Panel (i) plots the geomagnetic TEC map with gray contours at the top 1% value of TEC in the map, defining the High Density Regions (HDR). Panel (ii) isolates these HDRs and plots them in black. Panel (iii) shows the binary image of the HDRs with green contours drawn around each black region to demonstrate the algorithm's contour detection. Panel (iv) plots the isolated HDRs in SM coordinates with bounding rectangles in blue and centroids marked in black, obtained by the detection/tracking algorithm. Sub-figure (b) demonstrates the labeling process for consecutive images for the date 2013 − 04 − 02 from 09 : 30 : 00 to 10 : 15 : 00 UTC. Dashed lines connect the same labeled HDRs between images, with different colors for each unique HDR.

4.1. HDR Detection and Tracking

Figure 4a (i) plots the 0.99 quantile threshold on a geomagnetic TEC map in gray. Each $(\text{MLT}, \varphi_{\text{SM}})$ grid enclosed by these contours defines an HDR. We plot only these grids in Figure 4a (ii) to isolate HDRs from the rest of the map. This reduces the original TEC map to a black and white image, where black defines HDRs and white is the background.

HDRs in each image are detected with a contour finding function from OpenCV. Figure 4a (iii) plots green contours around each black region to demonstrate the process. From the contour data we calculate the centroid location, area and the size of the HDR in MLT and magnetic latitude. These are in units of pixels, Appendix A2 outlines the transformation into geomagnetic coordinates $(\text{MLT}, \varphi_{\text{SM}})$. The TEC average, maximum and sum is calculated for each HDR detected.

To track HDRs in time we first assign a unique label to each of the HDRs in each image. We then take images i and $i + 1$ and overlay them to test for HDRs that overlap between the two images; if there is an overlap detected, the label for the HDR in image $i + 1$ is matched to the overlapping HDR in image i. Any HDRs that have multiple overlaps or label changes arise from splitting and merging HDRs respectively. For these instances we assign the largest HDR in image $i + 1$ the label corresponding to the largest HDR that overlaps it in image i. All other overlapping HDRs in image $i + 1$ are assigned a new unique label. Figure 4b demonstrates the labeling process for four example date-times on $2013 - 04 - 02$ from $09:30:00$ UTC to $10:15:00$ UTC. We repeat this across the sequence of 20-year of images at a 15-min cadence, giving a data set of 110385 unique, contiguous space-time HDRs. Figure 4a (iv) shows HDRs plotted in geomagnetic coordinates with marked centroids and bounding rectangles to demonstrate the functionality of our algorithm. The results of this data set provide information on HDR path, duration and size, explored in the next section.

4.2. Ordering HDRs by Geomagnetic Activity and Area

Having obtained a data -set of uniquely labeled HDRs, we first bin the data by geomagnetic activity using the Kp index, which takes values between 0 and 9 and is derived from a global array of ground-based magnetometers (Alcay & Gungor, 2020). We divide the HDR data -set into three groups: quiet ($\text{Kp} < 4$), moderate ($4 \leq \text{Kp} < 7$) and extreme ($\text{Kp} \geq 7$) (Hanslmeier, 2002; Palacios et al., 2017). An HDR is assigned a Kp range based on the maximum Kp of its corresponding TEC maps during its lifetime. Kp data is taken from the NASA OMNIWeb archive (see Data Sources). Since this is a 3-hr index, each map within those 3-hr intervals share the same Kp value. Appendix C shows how using other indices such as Dst compare to Kp.

We next bin the data by HDR size: Figure 5 plots histogram distributions of the largest HDR area for (a) all the data and (b) different seasons for the calendar years (i) 2003, (ii) 2009, (iii) 2014 and (iv) 2020. These histograms are found to be bimodal in form, independent of season, year and activity. We will analyse HDRs as two distinct populations as shown in the bottom panel of Figure 5a—Small and Large, the latter group described by HDRs that exceed an area of $8.0 \times 10^6 \text{km}^2$ at some point in their lifetime. Given that the ground stations are generally land-based, this splits the data into HDRs that reach an area of roughly continental scale and HDRs that for their lifetimes have an area smaller than this. Small HDRs have approximately an exponential size distribution, while large HDRs have an approximately Gaussian size distribution with a sample mean $\bar{A}_{\text{Large}} \approx 8.4 \times 10^6 \text{km}^2$ and standard deviation $\sigma_{\text{Large}} \approx 0.2 \times 10^6 \text{km}^2$. The largest HDR reaches $A_{\max} \approx 1.1 \times 10^7 \text{km}^2$. Figure 5b shows that small and large HDRs follow distributions that vary weakly with season and level of geomagnetic activity. For spring, autumn and winter there are fewer continental-scale HDRs during solar maximum years (2003 and 2014) than during solar minimum years (2009 and 2020).

The data coverage spans latitudes from $\sim 70°$S to $45°$N. For high latitudes (beyond $\pm 50°$) there are 24 HDRs detected ($\sim 0.02\%$ of the data). Magnetic coordinates at higher latitudes are also not as well-defined as they are near the magnetic equator (Laundal & Richmond, 2017; Niehof et al., 2022). Thus we concentrate our analysis between latitudes of $\pm 50°$ (mid to low latitudes), focusing on EIA-like structures. This gives 110361 unique HDRs for analysis.

5. The Dynamics of HDRs

5.1. HDR Trajectories in Geomagnetic Coordinates

The dynamics of the centroids of both the small and large HDR populations during quiet, moderate and extreme levels of activity are plotted in Figure 6. Each trajectory is color-coded by peak HDR area and a filled circle marks the termination of each trajectory. If an HDR persists on one map only (duration $\tau < 15$ min) then a filled circle is plotted, which occurs for $\sim 23\%$ of the data. On each panel we give the sample size, which changes between different size groups and activity levels; of the 110361 HDRs identified, approximately 90.4% lie completely within $\text{Kp} < 4$, 9.3% reach the range $4 \leq \text{Kp} < 7$ and only 0.3% exist in maps with $\text{Kp} \geq 7$. Below and to the right of each axis we plot stacked histograms of the coordinates where HDRs form in MLT and magnetic latitude respectively. These are also colored by peak HDR area.

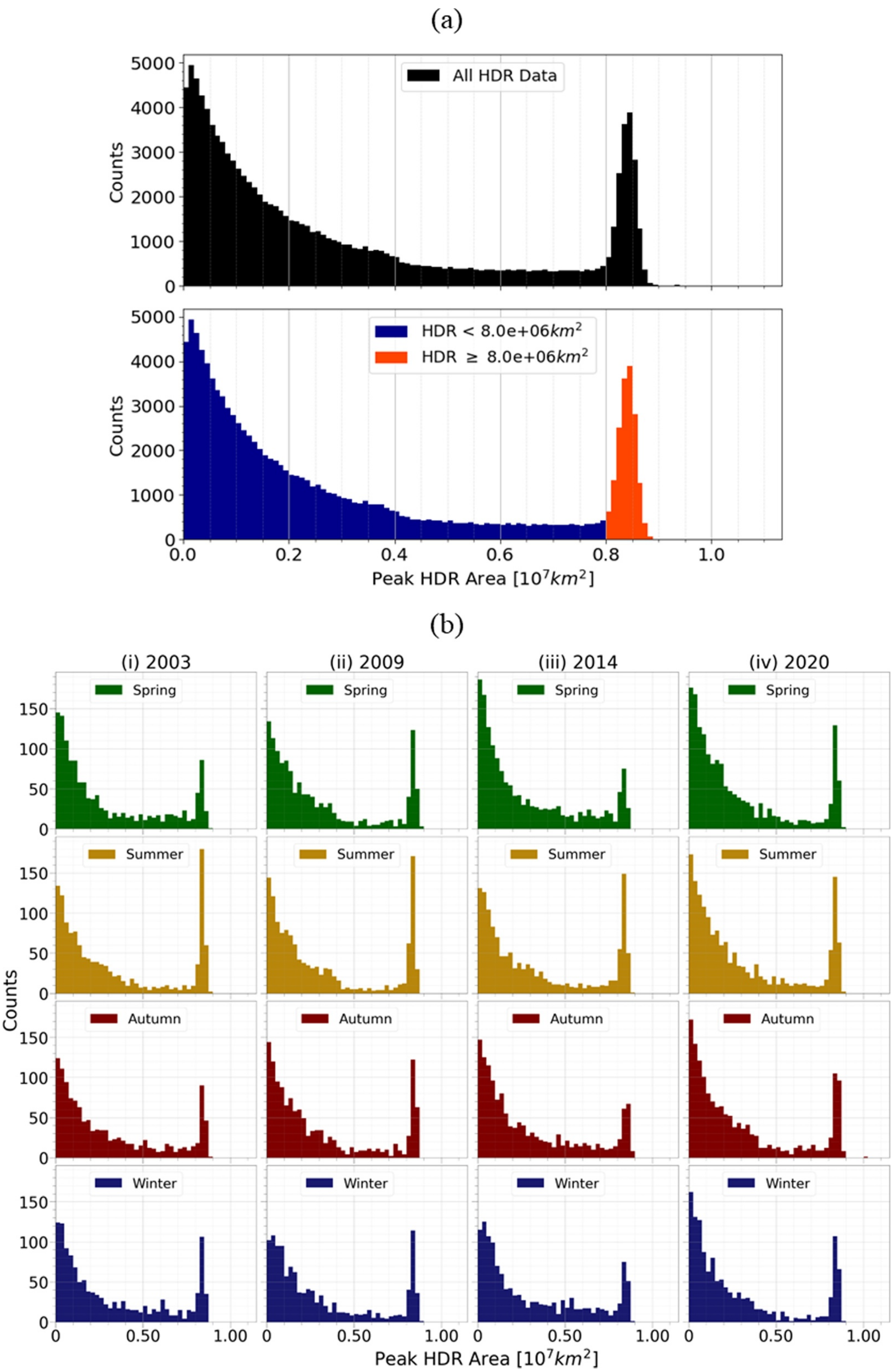

Figure 5. Sub-figure (a) plots distributions of the maximum area for each unique HDR in the data -set. The upper panel plots all the data and the bottom plots the distribution split into large (orange) and small (blue) HDRs, separated by an area of $8 \times 10^6 \mathrm{km}^2$. Sub-figure (b) plots these area distributions divided by for calendar years (i) 2003, (ii) 2009, (iii) 2014 and (iv) 2020. Histograms are normalized to integrate to 1.

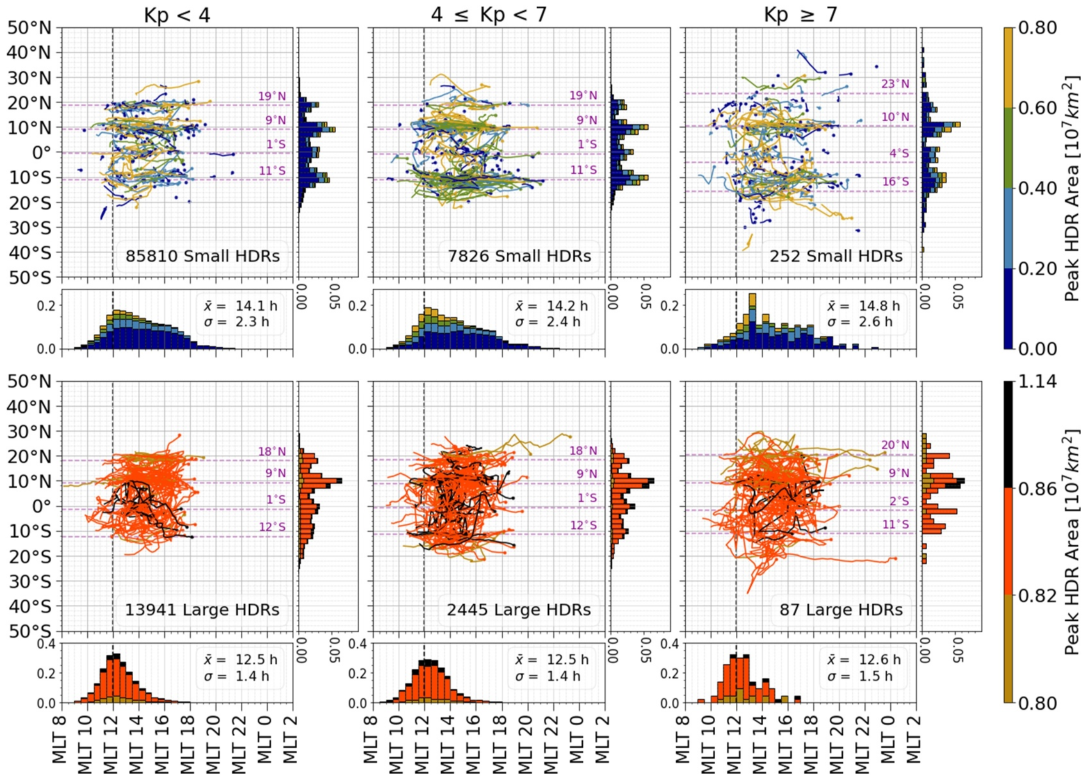

Figure 6. HDR trajectories plotted in SM coordinates. Each panel plots HDR paths for each label at different levels of Kp. The top row plots small HDRs and the bottom row plots large HDRs. Each column shows HDRs that occur during different activity levels, labeled at the top. Path endings are indicated by a filled circle. For Kp < 7 line plots are a sample equal to the number of HDRs in the extreme case. Paths are colored based on peak HDR area for that duration, with color-bars provided on each row. MLT 12 is marked with a black dashed vertical line for each panel. Horizontal purple dashed lines at constant latitude mark K-means centroids for each of the four clusters found, labeled with the calculated magnetic latitude value. PDFs for the location at which HDRs form in MLT and magnetic latitude are plotted alongside each panel along the relevant axes. They are colored based on the peak HDR area. The histograms are normalized to integrate to 1. The sample mean $\bar{x}$ and standard deviations σ for MLT distributions are given in legend of these panels in hours.

The locations at which small HDRs form is concentrated around four magnetic latitudes for all levels of activity. Using K-means clustering (see Python Packages section for documentation (Pedregosa et al., 2011)), we can approximate the mean position of these populations. In general these are found at $\varphi_{\mathrm{SM}} \sim 10°$S, $\sim 0°$, $\sim 10°$N and $\sim 20°$N. For $\mathrm{Kp} \geq 7$ these HDR formation points spread out toward higher latitudes, increasing the absolute value of the calculated K-means centroid for these latitudes. The largest population, which is $31 - 36\%$ of the small HDR data, form around 10°N. The cluster around 10°S contains $30 - 34\%$ of the data, $21 - 22\%$ form around the equatorial cluster and $13 - 14\%$ form in around 20°N. These percentages are independent of geomagnetic activity. In MLT the mean position at which small HDRs first form lies within MLT $14 - 15$, however the peaks of the distributions are skewed toward MLT 12. The standard deviation of these distributions spans $2.3 - 2.6$ hours in MLT. Both the sample mean and standard deviation increase with geomagnetic activity.

The large HDRs also form at locations concentrated around four clusters in magnetic latitude, however particularly for $\mathrm{Kp} < 4$ we see the distribution appears smoother over lower latitudes when compared to small HDRs—trajectories in the main panel are less ordered by magnetic latitude. The most concentrated cluster is around 10°N, comprised of $37 - 40\%$ of the large HDR data. For large HDRs with $\mathrm{Kp} \geq 7$ the cluster around 10°S only contains $\sim 6\%$ of the data, indicating a preference for northern hemisphere production of these HDRs. In MLT the histogram distribution for where HDRs form are narrower than for small HDRs, with a standard deviation of $1.4 - 1.5$ hr, and peak around the sample mean of ~MLT 12.5.

The seasonal dependence of the locations at which HDRs form is shown in Figure 7. The left-hand plots show the distributions of where the HDRs form separated by spring and autumn and different levels of geomagnetic

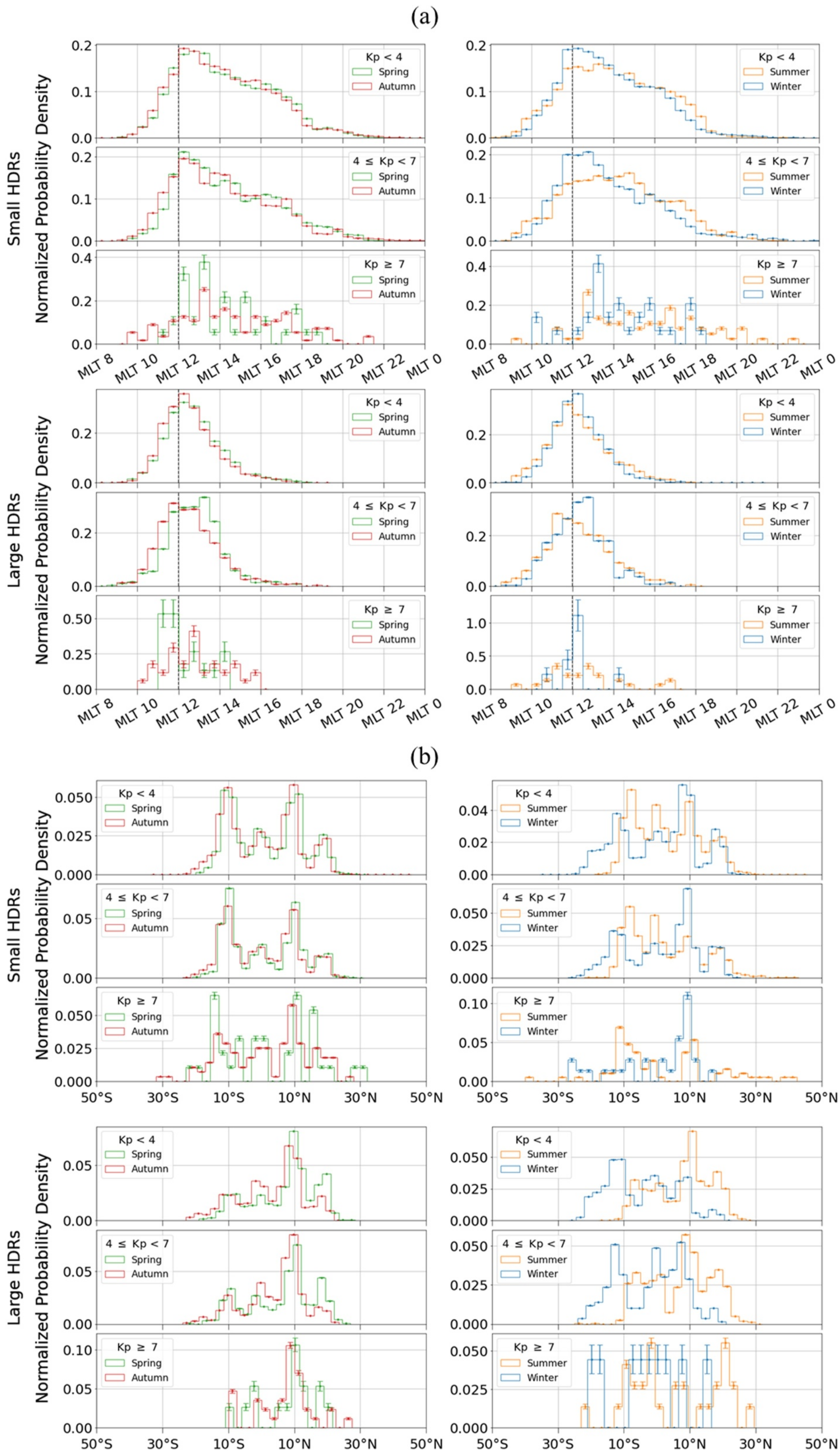

Figure 7. Seasonal histograms for the coordinates where HDRs first form. Sub-figure (a) plots MLT and sub-figure (b) plots the magnetic latitude. MLT 12 is marked as dashed lines in each panel of (a). The top group of each sub-figure plots small HDRs and the bottom group plots large HDRs. Each row plots data within a given Kp range, denoted in the legend. Spring/autumn are plotted on the left-hand column and summer/winter are plotted on the right-hand column. Error bars due to the sample size are plotted.

10.1029/2024SW004307

activity. We can see that the locations if HDR formation are insensitive to spring or autumn seasons for all HDR sizes and geomagnetic activity levels. The right-hand plots show the distributions of where HDRs form separated by summer and winter and different levels of geomagnetic activity. The formation latitude, and to a lesser extent MLT, are sensitive to summer or winter seasons. This is most apparent in the large HDRs and in the latitude of the formation point, where the trend is consistent with the seasonal variation of the sub-solar point latitude (Mendillo et al., 2005). Each distribution plots error bars showing the sample error, calculated from the sample standard deviation for each season's data (Hughes & Hase, 2010). These are very small for Kp < 7 but increase noticeably for Kp ≥ 7 due to the significantly smaller sample sizes from all seasons.

5.2. Magnetic Bearing of Net HDR Motion

Results from Figures 6 and 7 suggest that the location of TEC enhancement formation is partially but not completely controlled by the sub-solar point. We now test the idea that the subsequent HDR trajectories after formation are simply ordered by a combination of Earth rotation and magnetic confinement of the HDR such that the HDR remains at constant magnetic latitude (motion is parallel to the MLT axis). For this we consider the magnetic bearing; given the start coordinates (λ_1, φ_1) and end coordinates (λ_N, φ_N), where $N = \tau/15$ for some duration τ (in minutes), for an HDR centroid trajectory we can find the start-to-end separation vector $\mathbf{r}$ in geomagnetic longitude/latitude:

$$\mathbf{r} = (R_{\oplus} + h_{\text{iono}})\left[\Delta\lambda_{\text{SM}} \cos(\varphi_1)\hat{\mathbf{\Lambda}} + \Delta\varphi_{\text{SM}}\hat{\mathbf{\Phi}}\right] \tag{2}$$

where $R_{\oplus}$ is the Earth radius, h_{iono} is the altitude of the ionosphere, $\Delta\lambda_{\text{SM}}$ and $\Delta\varphi_{\text{SM}}$ are the change in geomagnetic longitude/latitude and $\hat{\mathbf{\Lambda}}$ and $\hat{\mathbf{\Phi}}$ are the unit vectors in magnetic longitude/latitude. The factor of $\cos(\varphi_1)$ arises from the curvature of the Earth taken with respect to the starting latitude of the HDR (Laundal & Richmond, 2017). We define the magnetic bearing β of an HDR trajectory as the clockwise angle from the geomagnetic latitude unit vector $\hat{\mathbf{\Phi}}$ to the separation vector $\mathbf{r}$:

$$\beta = \begin{cases} \cos^{-1}\left(\dfrac{\hat{\mathbf{\Phi}} \cdot \mathbf{r}}{|\mathbf{r}|}\right) & \Delta\lambda_{\text{SM}} \geq 0 \\ 360^\circ - \cos^{-1}\left(\dfrac{\hat{\mathbf{\Phi}} \cdot \mathbf{r}}{|\mathbf{r}|}\right) & \Delta\lambda_{\text{SM}} < 0 \end{cases} \tag{3}$$

Motion exactly parallel to MLT corresponds to $\beta = 90^\circ$ or $\beta = 270^\circ$. We require a start and end point in the trajectory to define a path, meaning only HDRs with durations exceeding and including $\tau = 15$ minutes are accounted for. This gives 84775 unique HDRs (77% of the whole data).

Figure 8 plots log-scaled distributions of the magnetic bearings for small and large HDRs under different levels of geomagnetic activity and binned by their formation location. The blue and orange bars represent small and large HDRs respectively. Magnetic latitude bearings $\beta = 90^\circ$ and $\beta = 270^\circ$ are indicated with vertical yellow lines. The majority of the HDRs have trajectories with bearings close to $\beta = 90^\circ, 270^\circ$ (yellow vertical lines), found within $\pm 15^\circ$ as shown by gray shaded regions. The motion of these HDRs is essentially parallel to lines of constant geomagnetic latitude. The population with $\beta = 90^\circ \pm 15^\circ$ is approximately an order of magnitude greater than that with $\beta = 270^\circ \pm 15^\circ$ for small HDRs, and approximately two orders of magnitude for large HDRs. This is seen for all levels of geomagnetic activity; for Kp ≥ 7 the distribution is not smooth, though the majority of bars are in/around the shaded horizontal regions. Calculating the percentage of data within the shaded regions we find $65 - 75\%$ of small HDRs and $80 - 83\%$ of large HDRs have a net trajectory parallel to MLT. This primarily consists of HDRs co-located with a fixed magnetic field line footprint that are moving in the sense of Earth rotation (toward later MLT), with $61 - 72\%$ of small HDRs and $79 - 83\%$ of large HDRs moving with a net bearing of $\beta = 90^\circ \pm 15^\circ$. These percentages are independent of latitude, season and geomagnetic activity for Kp < 7, but fewer HDRs follow a net horizontal path for Kp ≥ 7.

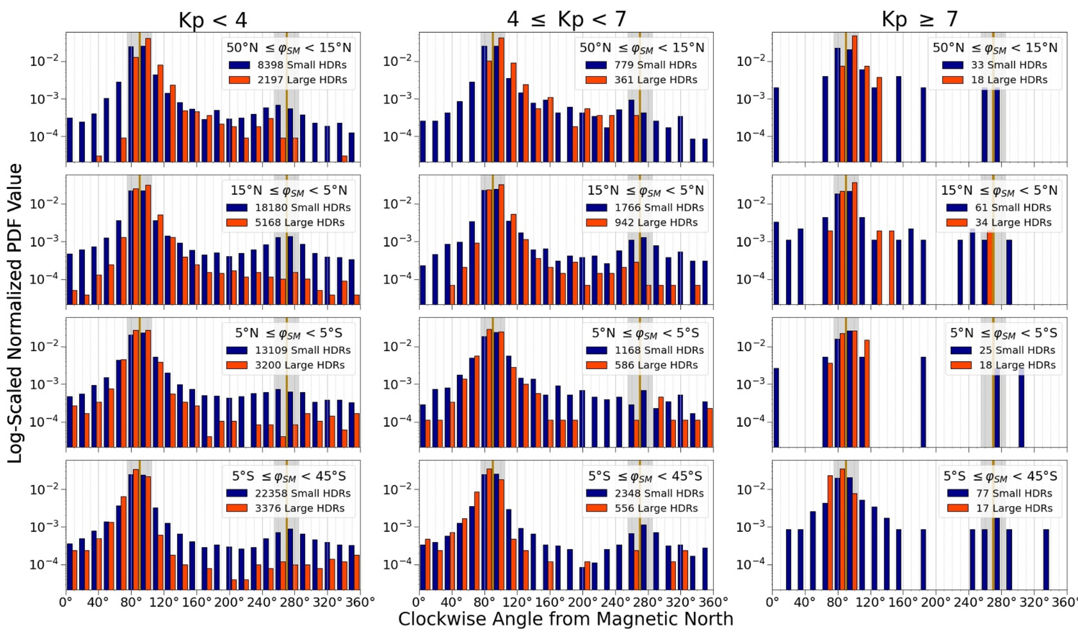

Figure 8. Log-scaled histogram plots of the magnetic bearing β, the clockwise angle from magnetic north, for large (orange) and small (blue) HDRs in 15° bins. The histograms are normalized to integrate to 1. Each panel plots net trajectory bearings within a latitude band for each K-means cluster determined in Figure 6 for different activity levels shown in each column. Legends in each panel indicate the latitude band and the number of small/large HDRs that form in these regions. The shaded regions ±15° from $\beta = 90°$ and $\beta = 270°$ indicate motion with approximately constant magnetic latitude. Only HDRs with durations $\tau \geq 15$ minutes are included.

5.3. Parameterizing the Straightness of Trajectories

In this section we will propose a new parameter which quantifies the extent in which a trajectory is ballistic or meandering. Having obtained this parameter we can then plot it against latitude and duration. Our analysis so far suggests an overall trend in HDR behavior: they primarily form between MLT 12 − 18 at four distinct magnetic latitudes partially influenced by the sub-solar point location. Subsequent net motion of HDRs shows a high proportion moving at these latitudes toward positive MLT. This would suggest close to ballistic (straight-line) trajectories for HDRs. We now quantify the extent to which the trajectories of the HDRs are ballistic: We introduce a ballistic parameter ζ as the ratio between the start-to-end separation distance $|\mathbf{r}|$ and the total path distance $d = \sum_{i=1}^{N} |\mathbf{r}_i|$ (the sum of all pairwise separations for $N = \tau/15$ points in the trajectory, where τ is the duration in minutes):

$$\zeta = \frac{|\mathbf{r}|}{d} \tag{4}$$

This is defined such that as $\zeta \rightarrow 1$ the path tends toward a straight line between the start and end HDR coordinates and as $\zeta \rightarrow 0$ the path increasingly deviates from the separation vector ($d \gg |\mathbf{r}|$). HDRs that appear on only one map ($\tau < 15$ minutes) will have no path (thus $d = 0$ and ζ is undefined) and HDRs that persist across two maps will always execute a straight line between start and end coordinates ($\zeta = 1$). We then consider HDRs with durations $\tau \geq 30$ min of which there are 71235 unique HDRs (65% of the full set of HDRs).

Figure 9a plots the magnetic latitude where an HDR forms versus ζ for small and large HDRs under different levels of geomagnetic activity. Each point is colored by duration, represented by the color-bar, and are plotted such that the shortest durations are plotted first and longer durations are over-plotted. Small HDRs on average last for around 2.75 − 3.75 hr and at most last ~1.5 days, whereas large HDRs on average last for around 10.25 − 11.25 hr and can persist for at most ~2.5 days. The longest durations occur under quiet geomagnetic conditions. Moreover, the longest-lived HDRs tend to form within the ±10° clusters in magnetic latitude, particularly for small HDRs.

10.1029/2024SW004307

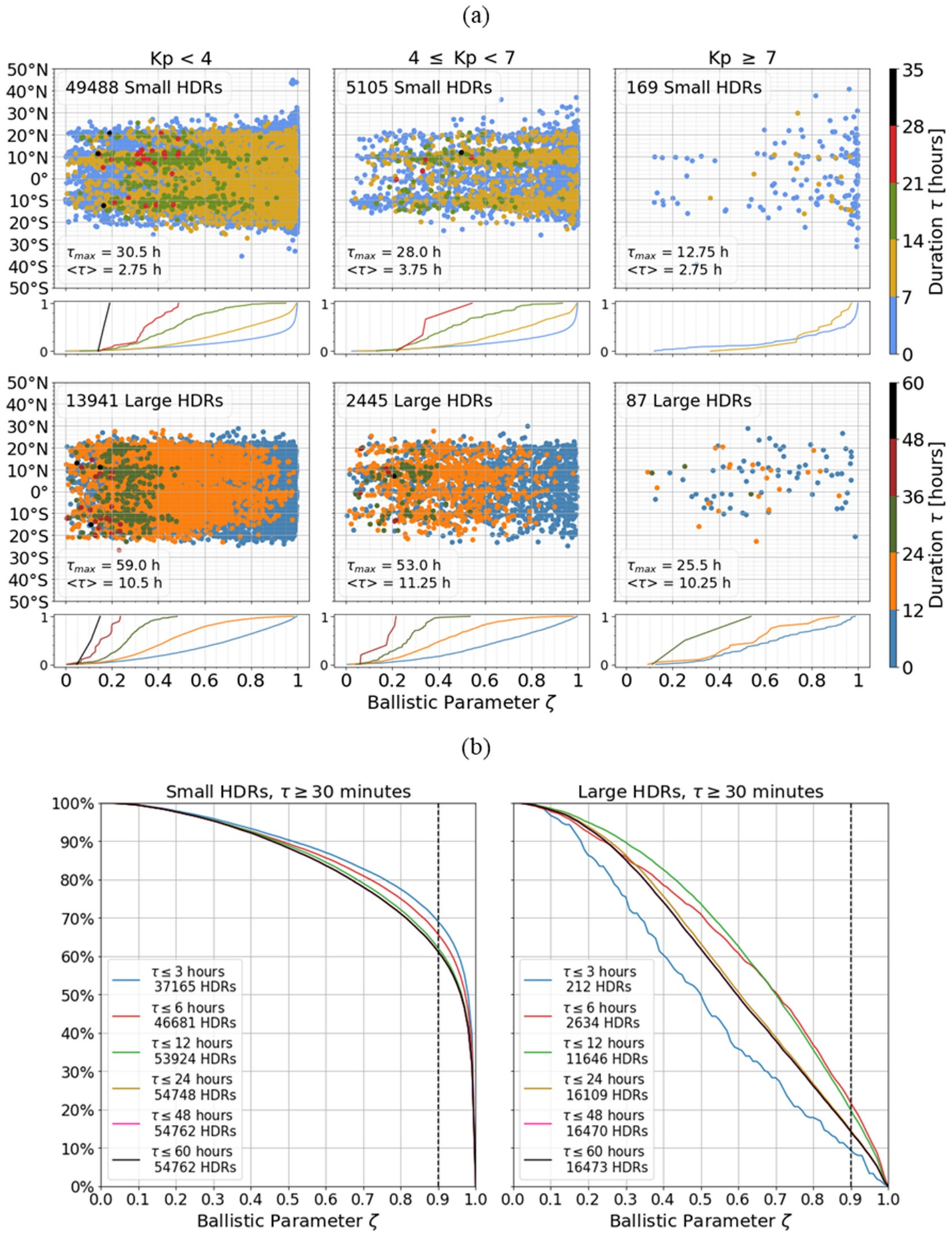

Figure 9. Sub-figure (a) plots the magnetic latitude of HDR formation plotted against the ballistic parameter ζ. The top row plots results for small HDRs and the bottom row for large HDRs. Each point is colored by the duration τ of the HDR, colorbars provided on each row, and the smallest durations are plotted underneath the longest durations. The number of HDRs and the maximum/average durations are shown in each axis. Below each axis the CDFs are plotted for ζ colored based on the duration bands defined by the color bar. Only HDRs with durations $\tau \geq 30$ minutes are plotted. Sub-figure (b) plots the percentage of HDRs that exceed a given value of ζ for small (left panel) and large (right panel) HDRs with durations $\tau \leq 3, 6, 12, 24, 48$ and 60 hr. The number of HDRs within each data sub-set is shown in the legend for each axis. Vertical dashed lines indicate the choice in ζ above which an HDR is defined to follow a ballistic trajectory.

Beneath each panel in Figure 9 plots the CDF for ζ for each duration band defined by the color-bar. There is a general tendency for longer-lived HDRs to be more meandering (they have a lower value of ζ) for all sizes and levels of geomagnetic activity. We can quantify the number of HDRs that travel in a straight trajectory from start to finish, defined as ballistic motion, by the criterion $\zeta \geq 0.9$. We plot the percentage of HDRs that exceed a given value of ζ in Figure 9b for small and large HDRs with durations at most $3, 6, 12, 24, 48$ and 60 hr (where 60 hr is the maximum measured duration, thus representing all HDRs with $\tau \geq 30$ minutes). Small HDRs show that the percentage of longer-lived HDRs following ballistic trajectories decreases. This trend is not clearly seen in large HDRs with duration $\tau \leq 3$, and to some extent those with duration $\tau \leq 6$ hr, as the sample size is significantly smaller than other duration bands. For HDRs of duration approximately $\tau \geq 24$ hr the percentage of ballistic HDRs follows the same trend. We focus on HDRs of 12 hr durations or less to determine the prevalence of ballistic trajectories, with $\zeta \geq 0.9$ as our condition for ballistic motion we find that 62% of small HDRs and 20% of large HDRs follow straight-line trajectories.

6. Discussion

6.1. Sub-Structures of EIAs From Quantile Analysis

The clustering in magnetic latitude in Figure 6 demonstrates a possible four-peak EIA structure for low latitudes. The organization of the formation point of the HDRs into these latitude bands favors HDR production at the $\pm 10°$ latitudes, consistent with studies such as Meng et al. (2024) and Dunn et al. (2024). This suggests a primary mechanism for EIA formation to be $\mathbf{E} \times \mathbf{B}$ drifts producing enhanced electron regions at these latitudes, consistent with existing research (Balan, Liu, & Le, 2018; Balan, Souza, & Bailey, 2018; Sparks et al., 2021). The other two clusters have been seen previously (Cai et al., 2022; Fathy & Ghamry, 2017; L. Huang et al., 2014; Y. Huang et al., 2024; Maruyama et al., 2016). Possible drivers for these clusters were discussed, concluding that the likely cause was from thermospheric winds carrying plasma to these regions from both mid and low latitudes. Equatorial EIAs could be as a result of the $\pm 10°$ enhancement pair merging around the equator, forming one large enhancement. This may explain the smoother histogram distribution seen for large HDRs during quiet geomagnetic conditions in Figure 6, where the four-peak structure begins to disappear. Large HDRs also show a sharper peak at the 10°N cluster in Figure 6, which indicates a preference for northern hemisphere production of large-scale TEC enhancements independent of the Kp range. This could be a feature of ground station coverage, where Figure 1a and Mannucci et al. (1998) show substantially more ground stations and hence better coverage for the northern hemisphere.

Our results may also depend on the thresholding used in our analysis, see Appendix B: by setting the HDR threshold to be at a fixed quantile of TEC values per map, the threshold value of TEC tracks the overall season and solar cycle variation as shown in Figure 3. Under more active geomagnetic conditions it is possible that not all of the EIA seen in other studies will be resolved at the 0.99 quantile—smaller HDRs for higher Kp might be sub-structures all part of a wider EIA that has similar boundaries to those detected at quieter times (see Nikitina et al. (2022) for suggested thresholds of TEC for different latitude bands and activity levels). This suggests that the HDR area can potentially contain information about the spatial structure within EIA TEC enhancement regions, possibly explaining the natural divide in the area distributions from Figure 5. The functional form of the HDR size distributions will in part depend on the specific methodology used to identify the TEC threshold which defines the HDRs. Here, the 0.99 quantile was used in order to explore the high values of TEC that form over a range of geomagnetic activity. Detailed physics questions, such as defining the full EIA structure, or specific practical applications may have different requirements for HDR selection. The methodology developed here, and the results can provide the basis for such studies.

6.2. Uncertainties in GIM Observations

The results from this study are all based on one of the JPL GIM products: the JPLD TEC maps, produced every 15 min for the years 2003–2022 (Meng & Verkhoglyadova, 2023). Issues arise with the accuracy of the maps, which are heavily reliant on the distribution of GNSS ground-based receivers seen in Figure 1a. Caution is needed for HDRs that are "detected" over the oceans, where TEC data is purely statistical, but over continents we assume the data is reliable. Meng et al. (2024) showed that 75% of TEC intensifications they detected contained at least two receivers and 90% contained at least one. Although these enhancements were obtained from a slightly different method to this study (use of a Laplacian over a quantile threshold), their results suggest that data from these GIMs offered reliable representations of TEC enhancements. Given the length of the data -set (20 years), we have comprehensive coverage of all MLT, seasons and activity levels with a high density of ground stations. This is also in agreement with other studies using different TEC estimation methods (Astafyeva et al., 2008; Amiri-Simkooei & Asgari, 2012; Badeke et al., 2018; Knudsen, 2022) and with our TEC variability results from Figure 3. It is then reasonable to conclude that despite smoothing of TEC over undefined regions, the overall TEC behavior at the extremes is still captured in the maps. The comparison of GIMs with independent measurements showed a typical error <3 TECU outside of high latitudes (Roma-Dollase et al., 2018). This is also carried out over oceans (with space altimeters). This result is in agreement with detailed analysis of JPLD data product error in Martire et al. (2024). Furthermore, Maruyama et al. (2021) and Xiong et al. (2022) tested the response of TEC on maps produced using spherical harmonics and showed diurnal, latitudinal and geomagnetic activity sensitivities in agreement with results found in Figure 3. It may be useful to compare the statistics of HDR dynamics using different types of maps to the results from JPL GIMs in this study in a similar analysis as Roma-Dollase et al. (2018) to further test consistency between current TEC map products.

Another limitation to the analysis arises from sample size variations between geomagnetic activity and season—HDRs when $\mathrm{Kp} \geq 7$ is about 0.3% of the 20-year data set, whereas HDRs with $\mathrm{Kp} < 4$ is about 90.4%. This difference in sample size will always be the case regardless of the number of solar cycles we analyse, since extreme geomagnetic events are rare in comparison to quiet conditions (Nikitina et al., 2022). However by considering the number of samples available from this data set it is clear that for a comprehensive analysis on TEC extremes we require more TEC data to determine the statistics of HDRs with $\mathrm{Kp} \geq 7$ more reliably. This is even more apparent if we are to consider seasonal affects to these HDRs, where splitting the data by season reduced the sample size to as low as 10 HDRs for winter months. With just two solar cycles it is difficult to decisively conclude how seasons affect our results for high geomagnetic activity, shown by Figure 7 where the error bars for the $\mathrm{Kp} \geq 7$ histograms are substantial.

7. Conclusions

We have studied the dynamics of TEC enhancements in $1^\circ \times 1^\circ \times 15$ min global ionospheric TEC maps provided by JPL between 2003 and 2022. Maps were converted to a geomagnetic coordinate frame to analyse TEC behavior with respect to the sub-solar point and the Earth's magnetic field. A fixed quantile threshold was defined for each map and was used to identify TEC enhancements. An algorithm was developed to detect and track these regions, providing the centroid location, area, TEC intensification, duration and path of unique HDRs for magnetic latitudes between $\pm 50^\circ$. The main findings are:

- The 0.99 TEC quantile threshold is sensitive to Earth/Solar rotation, season and solar cycle.
- The distribution of peak HDR area naturally separates the HDRs into small and large area at $8.0 \times 10^6 \mathrm{km}^2$, roughly at the continental-scale.
- Small HDRs on average are found to form at MLT $14-15$ for all activity bands, while Large HDRs on average form just after MLT 12. The HDR areas within both populations are largest around MLT $14-15$. The spread in MLT where the HDRs form is larger for small HDRs than for those at a continental-scale.
- The magnetic latitude at which HDRs form clusters around four populations, which are centered about $\varphi_{\mathrm{SM}} \approx 10^\circ$S, 0°, 10°N & 20°N. The majority of HDRs form within the $\pm 10^\circ$ clusters.
- Small HDRs cluster at later MLT in summer and earlier MLT in winter. In winter, all HDRs cluster more toward southern hemisphere latitudes, and more towards the northern hemisphere in summer. For spring/autumn the distributions of HDRs are indistinguishable from each other for all sizes.
- $61-72\%$ of small HDRs and $79-83\%$ of large HDRs move on trajectories that are within $\pm 15^\circ$ of constant magnetic latitude and are directed toward later MLT. This is independent of the latitude cluster an HDR is formed in. We find the lowest number of horizontally moving HDRs for higher Kp.
- Small HDRs on average last between $2.75-3.75$ hours and at most last for ~ 1 day. Large HDRs on average last between $10.25-11.25$ hours and at most exist for ~ 2.5 days.
- The longest duration HDRs for both populations tend to form within the clusters located around $\pm 10^\circ$ magnetic latitude, with the HDR duration decreasing with increasing activity.
- Shorter-lived, small HDRs tend to have ballistic trajectories, where for durations $0.5 \leq \tau \leq 12$ hours 62% have a value of $\zeta \geq 0.9$. Large HDRs have more complex meandering paths, where only 20% with durations $\tau \leq 12$ hr have a value of $\zeta \geq 0.9$.

10.1029/2024SW004307

Our analysis has considered the dynamics of large-scale TEC enhancements at the 0.99 quantile of global ionospheric maps and showed how their statistics depend on latitude, season and geomagnetic activity. HDR formation is shown to be partially influenced by the sub-solar position, typically forming at four latitude bands spanning the afternoon ionosphere. The majority of HDRs in general move roughly parallel to lines of constant magnetic latitude toward later MLT, that is, the HDRs are co-located with a fixed magnetic field line footprint that are moving in the sense of Earth rotation. Small, short-lived HDRs tend to have ballistic trajectories, while large, longer-lived HDRs tend to have more meandering trajectories. Further work that is tailored to the specific requirements of the user community could usefully refine the parametrization used here, specifically the quantile threshold for HDR identification and the ballistic parameter. The statistical trends seen in these ionospheric HDRs provide a benchmark which can be compared to ensembles of the outputs of detailed ionospheric modeling. Our study also provides necessary information and a tool to create training and testing data sets for AI-based model development (Poduval et al., 2023).

Appendix A: Coordinate Transformations

A1. Solar Magnetic Coordinates

The SM coordinate system defines an orthonormal basis with basis vectors $\hat{\mathbf{m}}$ (the Earth magnetic dipole field vector), $\hat{\mathbf{m}} \times \hat{\mathbf{s}}$ (where $\hat{\mathbf{s}}$ is the sub-solar vector pointing from the Earth to the Sun) and a cross product of these two vectors (Jursa, 1985; Laundal & Richmond, 2017). The magnetic longitude and latitude are defined from these basis vectors. We express magnetic longitude in terms of Magnetic Local Time (MLT) in our maps:

$$\mathrm{MLT} = \frac{\lambda - \lambda_{\hat{\mathbf{s}}}}{15} + 12 \tag{A1}$$

for a given longitude λ and sub-solar point longitude $\lambda_{\hat{\mathbf{s}}}$. This definition is universal for any magnetic coordinate system (Laundal & Richmond, 2017). For SM coordinates $\lambda_{\hat{\mathbf{s}}} = 0°$ for all times, fixing the sub-solar point in longitude to the center of our maps. This means $\lambda_{\mathrm{SM}} = 0°$ always corresponds to MLT 12.

A2. Conversions From Pixel Coordinates

HDR parameters derived from the algorithm in Section 4.1 are given in pixel units. The dimensions of each image is defined such that the pixel width W corresponds to the MLT axis, from MLT 0 to MLT 24, and the pixel height H corresponds to the magnetic latitude φ_{SM} axis, from $-90°$ to $90°$. We convert from pixel coordinates (x_p, y_p) into geomagnetic coordinates $(\mathrm{MLT}, \varphi_{\mathrm{SM}})$:

$$\mathrm{MLT} = x_p \times \frac{24}{W}, \quad \varphi_{\mathrm{SM}} = \left(y_p \times \frac{180}{H}\right) - 90 \tag{A2}$$

Each image is defined such that the image width $W = 720$ pixels and the image height $H = 360$ pixels. This is to ensure our image is large enough to identify smaller structures in the maps, but not too large as to introduce substantial errors to calculations.

Areas are calculated in square pixel units using OpenCV. Assuming a spherical thin-shell approximation of the ionosphere, we can derive a small area element on the surface of a sphere of radius r as $dA = r^2 \sin\theta d\theta d\phi$, where $\theta = 90° - \varphi_{\mathrm{SM}}$ is the co-latitude, $d\theta = \Delta\varphi_{\mathrm{SM}}$ the change in latitude and $d\phi = \Delta\lambda_{\mathrm{SM}}$ the change in longitude (Laundal & Richmond, 2017). For a given image width W and height H and using the conversions from Equation A2 we calculate the area of a 1×1 pixel on our global maps in km^2 as

$$A_{1\times1} = \frac{2\pi^2 (R_{\oplus} + h_{\mathrm{iono}})^2}{WH} \cos(\varphi_{\mathrm{cent}}) \tag{A3}$$

where $R_{\oplus}$ is the Earth radius, h_{iono} is the ionospheric altitude (set at $450 km$ for these maps (Lalgudi Gopalakrishnan & Schmidt, 2022; Mannucci et al., 1998; Wang et al., 2016)) and φ_{cent} is the magnetic latitude of an

HDR centroid. This conversion factor is multiplied by the area calculated using OpenCV to give the HDR area in km^2.

Appendix B: Isolated HDRs for Different Quantile Thresholds

We consider how varying the quantile threshold affects the size of HDRs detected in our algorithm. Figure B1 plots the isolated HDRs for the TEC map on $2009-07-23$ at $16:30:00$ UTC for different quantiles $q = 0.999, 0.99, 0.95, 0.90, 0.75$ and 0.50. Smaller structures seen when using higher quantile thresholds merge together at lower quantiles.

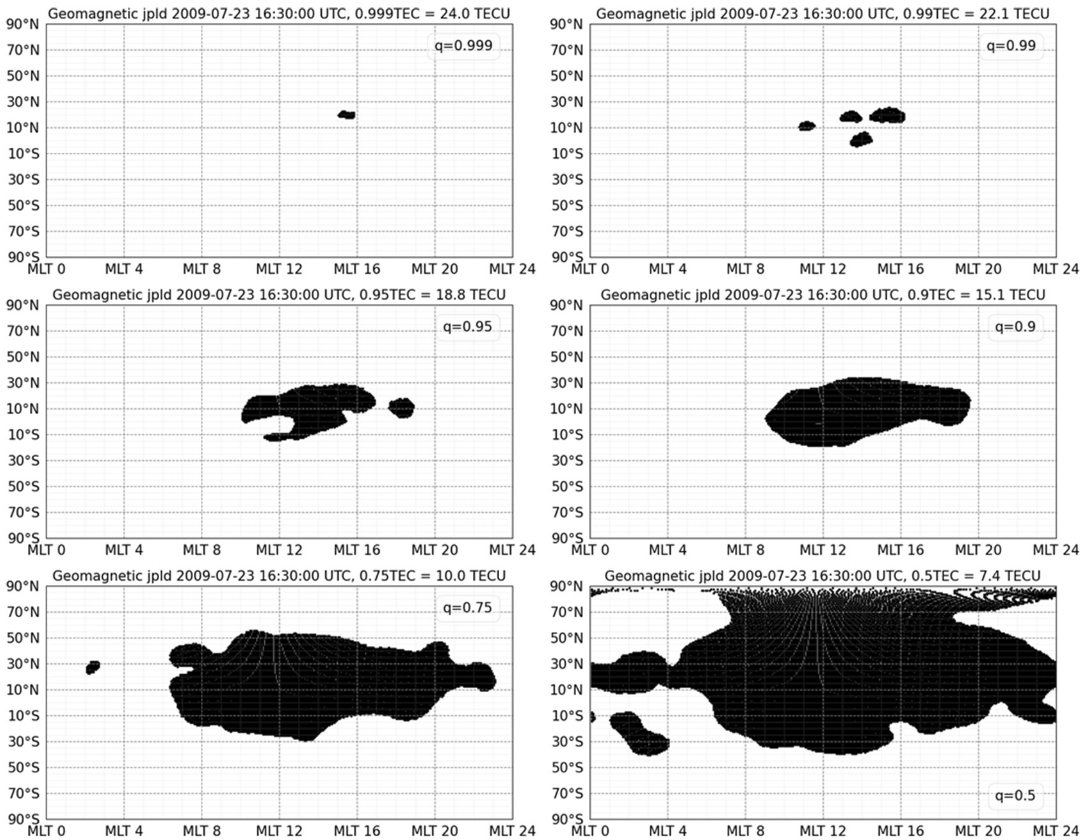

Figure B1. Isolated HDRs for the TEC map on $2009-07-23$ at $16:30:00$ UTC in geomagnetic coordinates using different quantile thresholds: $q = 0.999, 0.99, 0.95, 0.90, 0.75$ and 0.50. The value of TEC for these quantile thresholds is given in the title of each plot, along with the date and map type.

Appendix C: Comparing Kp to Dst

We use the Kp index to define the level of geomagnetic activity in the ionosphere, as Kp is widely used for this purpose (Matzka et al., 2021). Other geomagnetic indices can be used (Bergin et al., 2022, 2023; Wanliss & Showalter, 2006), for example, the hourly Dst index. Figure C1 plots the average and peak Dst in 3-hr intervals against Kp value between the calendar years 2003 and 2022. Dst data is taken from the NASA OMNIWeb archive (see Data Sources). Vertical dashed lines and the color of the points demarcate the ranges of Kp used to bin the data by geomagnetic activity. For the ranges covering quiet and moderate geomagnetic activity (blue and orange), that is $Kp < 7$, Dst changes slowly with Kp in a manner which is well within the vertical scatter of the plot. For $Kp \geq 7$ (red), Dst varies more strongly with Kp, however this variation is still within the vertical scatter.

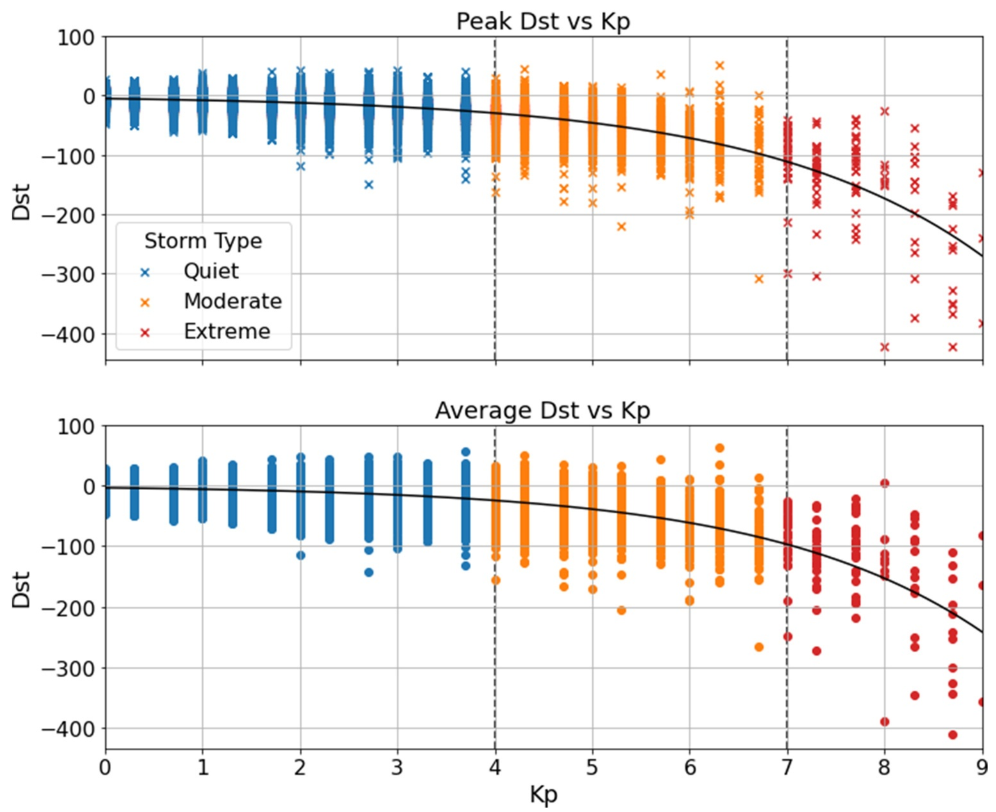

Figure C1. Peak/average hourly Dst over a 3-hr interval versus Kp. The plot is split between the three different storm conditions defined in Section 4.2: quiet (Kp < 4), moderate (4≤ Kp <7) and extreme (Kp ≥7). The bounds are indicated by vertical dashed lines and each storm type is color-coded as per the legend in the top panel. A fitted exponential curve is plotted in black.

Data Availability Statement

Data Sources. All data taken between 2003 − 01 − 01 and 2022 − 12 − 31.

- *JPL data*: https://sideshow.jpl.nasa.gov/pub/iono_daily/gim_for_research/jpld/, JPLD data used, created 2023 − 04 − 21. Note there is a missing day of data on 2003 − 10 − 30
- *Kp and Dst Index*: NASA OMNIWeb service, https://omniweb.gsfc.nasa.gov/form/dx1.html, downloaded 2023 − 08 − 16
- *Sunspot Data*: Silso, https://www.sidc.be/SILSO/datafiles, downloaded 2023 − 08 − 04.

Python Packages. All work was carried out in Python. A list of key Python packages from this work is given below, noting the version, documentation and the section of the analysis the package was used:

- Detection and Tracking algorithm: OpenCV, v4.7.0.72 (https://opencv.org/)
- Coordinate Transformations and the Sub-Solar Point: SpacePy, v0.4.1 (https://spacepy.github.io)
- Statistics and Time-Series analysis: SciPy, v1.10.1 (https://scipy.org)
- K-means clustering: scikit-learn, v0.24.1 (https://scikit-learn.org/stable/index.html)
- Station Coverage: PyProj, v3.4.0 (https://pyproj4.github.io/pyproj/stable/).

Acknowledgments
We acknowledge AFOSR/EOARD, Grant FA8655-22-1-7056, and the University of Warwick. A portion of research was carried out at the Jet Propulsion Laboratory, California Institute of Technology, under a contract with NASA.

References

Adkins, V. J., & England, S. L. (2023). Automated detection and tracking of equatorial plasma bubbles utilizing global-scale observations of the limb and disk (GOLD) 135.6 nm data. *Earth and Space Science*, *10*, e2023EA002935. https://doi.org/10.1029/2023EA002935

Alcay, S., & Gungor, M. (2020). Investigation of ionospheric TEC anomalies caused by space weather conditions. *Astrophysics and Space Science*, *365*(9), 150. https://doi.org/10.1007/s10509-020-03862-x

Amiri-Simkooei, A. R., & Asgari, J. (2012). Harmonic analysis of total electron contents time series: Methodology and results. *GPS Solutions*, *16*(1), 77–88. https://doi.org/10.1007/s10291-011-0208-x

Anthes, R. A. (2011). Exploring Earth's atmosphere with radio occultation: Contributions to weather, climate and space weather. *Atmospheric Measurement Techniques*, *4*(6), 1077–1103. https://doi.org/10.5194/amt-4-1077-2011

Aravindan, P., & Iyer, K. N. (1990). Day-to-day variability in ionospheric electron content at low latitudes. *Planetary and Space Science*, *38*(6), 743–750. https://doi.org/10.1016/0032-0633(90)90033-M

Astafyeva, E. I., Afraimovich, E. L., Oinats, A. V., Yasukevich, Y. V., & Zhivetiev, I. V. (2008). Dynamics of global electron content in 1998–2005 derived from global GPS data and IRI modeling. *Advances in Space Research*, *42*(4), 763–769. https://doi.org/10.1016/j.asr.2007.11.007

Badeke, R., Borries, C., Hoque, M. M., & Minkwitz, D. (2018). Empirical forecast of quiet time ionospheric Total Electron Content maps over Europe. *Advances in Space Research*, *61*(12), 2881–2890. https://doi.org/10.1016/j.asr.2018.04.010

Balan, N., Liu, L., & Le, H. (2018). A brief review of equatorial ionization anomaly and ionospheric irregularities. *Earth and Planetary Physics*, *2*(4), 257–275. https://doi.org/10.26464/epp2018025

Balan, N., Souza, J., & Bailey, G. J. (2018). Recent developments in the understanding of equatorial ionization anomaly: A review. *Journal of Atmospheric and Solar-Terrestrial Physics*, *171*, 3–11. https://doi.org/10.1016/j.jastp.2017.06.020

Bergin, A., Chapman, S. C., Moloney, N. R., & Watkins, N. W. (2022). Variation of geomagnetic index empirical distribution and burst statistics across successive solar cycles. *Journal of Geophysical Research: Space Physics*, *127*(1), e2021JA029986. https://doi.org/10.1029/2021JA029986

Bergin, A., Chapman, S. C., Watkins, N. W., Moloney, N. R., & Gjerloev, J. W. (2023). Extreme event statistics in Dst, SYM-H, and SMR geomagnetic indices. *Space Weather*, *21*(3), e2022SW003304. https://doi.org/10.1029/2022SW003304

Bilitza, D., Pezzopane, M., Truhlik, V., Altadill, D., Reinisch, B. W., & Pignalberi, A. (2022). The international reference ionosphere model: A review and description of an ionospheric benchmark. *Reviews of Geophysics*, *60*(4), e2022RG000792. https://doi.org/10.1029/2022RG000792

Bradski, G. (2000). *The OpenCV library*. Dr. Dobb's Journal of Software Tools. ID 2236121.

Buzulukova, N., & Tsurutani, B. (2022). Space Weather: From solar origins to risks and hazards evolving in time. *Frontiers in Astronomy and Space Sciences*, *9*. https://doi.org/10.3389/fspas.2022.1017103

Cai, X., Qian, L., Wang, W., McInerney, J. M., Liu, H.-L., & Eastes, R. W. (2022). Investigation of the post-sunset extra electron density peak poleward of the equatorial ionization anomaly southern crest. *Journal of Geophysical Research: Space Physics*, *127*(10), e2022JA030755. https://doi.org/10.1029/2022JA030755

Chen, P., Wang, R., Yao, Y., An, Z., & Wang, Z. (2022). On the global ionospheric diurnal double maxima based on GPS vertical total electron content. *Journal of Space Weather and Space Climate*, *12*, 38. https://doi.org/10.1051/swsc/2022035

Chen, Y., Liu, L., Le, H., Wan, W., & Zhang, H. (2016). Equatorial ionization anomaly in the low-latitude topside ionosphere: Local time evolution and longitudinal difference. *Journal of Geophysical Research: Space Physics*, *121*(7), 7166–7182. https://doi.org/10.1002/2016JA022394

Chen, Z., Zhang, S.-R., Coster, A. J., & Fang, G. (2015). EOF analysis and modeling of GPS TEC climatology over North America. *Journal of Geophysical Research: Space Physics*, *120*(4), 3118–3129. https://doi.org/10.1002/2014JA020837

Doherty, P., Coster, A. J., & Murtagh, W. (2004). Space weather effects of October–November 2003. *GPS Solutions*, *8*(4), 267–271. https://doi.org/10.1007/s10291-004-0109-3

Dunn, C., Meng, X., & Verkhoglyadova, O. P. (2024). Temporal variability of equatorial ionization anomaly crest locations extracted from global ionospheric maps. *Space Weather*, *22*(5), e2023SW003737. https://doi.org/10.1029/2023SW003737

Emmert, J. T., Mannucci, A. J., McDonald, S. E., & Vergados, P. (2017). Attribution of interminimum changes in global and hemispheric total electron content. *Journal of Geophysical Research: Space Physics*, *122*(2), 2424–2439. https://doi.org/10.1002/2016JA023680

Fathy, A., & Ghamry, E. (2017). A statistical study of single crest phenomenon in the equatorial ionospheric anomaly region using Swarm A satellite. *Advances in Space Research*, *59*(6), 1539–1547. https://doi.org/10.1016/j.asr.2016.12.020

Foster, J. (1993). Storm time plasma transport at middle and high latitudes. *Journal of Geophysical Research*, *98*(A2), 1675–1690. https://doi.org/10.1029/92JA02032

Hanslmeier, A. (2002). *The sun and space weather*. Kluwer Academic Publishers.

He, L., Zhu, Q., & Wang, C. (2024). Comprehensive analysis of the equatorial ionization anomaly based on global ionospheric maps with a high spatiotemporal resolution. *Advances in Space Research*, *74*(8), 3511–3526. https://doi.org/10.1016/j.asr.2024.06.047

Hernández-Pajares, M., Juan, J. M., Sanz, J., Aragón-Àngel, À., García-Rigo, A., Salazar, D., & Escudero, M. (2011). The ionosphere: Effects, GPS modeling and the benefits for space geodetic techniques. *Journal of Geodesy*, *85*(12), 887–907. https://doi.org/10.1007/s00190-011-0508-5

Huang, L., Wang, J., Jiang, Y., Huang, J., Chen, Z., & Zhao, K. (2014). A preliminary study of the single crest phenomenon in total electron content (TEC) in the equatorial anomaly region around 120°E longitude between 1999 and 2012. *Advances in Space Research*, *54*(11), 2200–2207. https://doi.org/10.1016/j.asr.2014.08.021

Huang, Y., Xiong, C., Wan, X., Park, J., & Spogli, L. (2024). The third plasma density peak at poleward of EIA crest: Swarm and ICON observations. *Journal of Geophysical Research: Space Physics*, *129*(4), e2023JA032035. https://doi.org/10.1029/2023JA032035

Hughes, I. G., & Hase, T. P. A. (2010). *Measurements and their uncertainties: A practical guide to modern error analysis*. Oxford University Press.

Immel, T. J., Sagawa, E., England, S. L., Henderson, S. B., Hagan, M. E., Mende, S. B., et al. (2006). Control of equatorial ionospheric morphology by atmospheric tides. *Geophysical Research Letters*, *33*(15), L15108. https://doi.org/10.1029/2006GL026161

Janssen, V. (2012). Likely Impact of the Approaching solar maximum on GNSS Surveys: Be alert but not alarmed. In *Proceedings of the 17th Association of Public Authority Surveyors Conference (APAS2012)*. Retrieved from https://www.spatial.nsw.gov.au/__data/assets/pdf_file/0006/169953/2012_Janssen_APAS2012_impact_of_solar_maximum_on_GNSS_surveys.pdf

Jehle, M., Rüegg, M., Small, D., Meier, E., & Nüesch, D. (2006). Comparison of different TEC map estimation methods. In *Proceedings of 13th Australasian Remote Sensing and Photogrammetry Conference (ARSPC)* (p. 6). Retrieved from https://www.researchgate.net/publication/233415577_Comparison_of_Different_TEC_Map_Estimation_Methods

Jursa, A. S. (1985). In *Handbook of geophysics and the space environment, 4th edition*. Air Force Geophysics Laboratory, Air Force Systems Command, US Air Force.

Keskinen, M. J., Ossakow, S. L., & Fejer, B. G. (2003). Three-dimensional nonlinear evolution of equatorial ionospheric spread-F bubbles. *Geophysical Research Letters*, *30*(16). https://doi.org/10.1029/2003GL017418

Kintner, P. M., & Ledvina, B. M. (2004). The ionosphere, radio navigation, and global navigation satellite systems. *Advances in Space Research*, *35*(5), 788–811. https://doi.org/10.1016/j.asr.2004.12.076

Knudsen, J. (2022). *Seasonal variations in global ionospheric total electron content*. Physics Capstone Projects. Paper 103 Retrieved from https://digitalcommons.usu.edu/phys_capstoneproject/103

Lalgudi Gopalakrishnan, G., & Schmidt, M. (2022). Ionospheric electron density modelling using B-splines and constraint optimization. *Earth Planets and Space*, *74*(1), 143. https://doi.org/10.1186/s40623-022-01693-4

Laundal, K. M., & Richmond, A. D. (2017). Magnetic coordinate systems. *Space Science Reviews*, *206*(1–4), 27–59. https://doi.org/10.1007/s11214-016-0275-y

Li, Z., Wang, N., Wang, L., Liu, A., Yuan, H., & Zhang, K. (2019). Regional ionospheric TEC modeling based on a two-layer spherical harmonic approximation for real-time single-frequency PPP. *Journal of Geodesy*, *93*(9), 1659–1671. https://doi.org/10.1007/s00190-019-01275-5

Lin, C. H., Richmond, A. D., Heelis, R. A., Bailey, G. J., Lu, G., Liu, J. Y., et al. (2005). Theoretical study of the low- and midlatitude ionospheric electron density enhancement during the October 2003 superstorm: Relative importance of the neutral wind and the electric field. *Journal of Geophysical Research*, *110*(A12), A12312. https://doi.org/10.1029/2005JA011304

Liu, J., Chen, R., Wang, Z., & Zhang, H. (2011). Spherical cap harmonic model for mapping and predicting regional TEC. *GPS Solutions*, *15*(2), 109–119. https://doi.org/10.1007/s10291-010-0174-8

Liu, J., Wang, W., Burns, A., Solomon, S. C., Zhang, S., Zhang, Y., & Huang, C. (2016). Relative importance of horizontal and vertical transports to the formation of ionospheric storm-enhanced density and polar tongue of ionization. *Journal of Geophysical Research: Space Physics*, *121*(8), 8121–8133. https://doi.org/10.1002/2016JA022882

Liu, J. Y., Yang, W. H., Lin, C. H., Chen, Y. I., & Lee, I. T. (2013). A statistical study on the characteristics of ionospheric storms in the equatorial ionization anomaly region: GPS-TEC observed over Taiwan. *Journal of Geophysical Research: Space Physics*, *118*(6), 3856–3865. https://doi.org/10.1002/jgra.50366

Liu, L., Wan, W., Ning, B., & Zhang, M.-L. (2009). Climatology of the mean total electron content derived from GPS global ionospheric maps. *Journal of Geophysical Research*, *114*(A6), A06308. https://doi.org/10.1029/2009JA014244

Luan, X. (2021). Equatorial ionization anomaly variations during geomagnetic storms. In C. Huang, G. Lu, Y. Zhang, & L. J. Paxton (Eds.), *Ionosphere dynamics and applications*. https://doi.org/10.1002/9781119815617.ch13

Lupsic, B., & Takacs, B. (2022). Gauss Process regression for real-time ionospheric delay estimation from GNSS observations. *Acta Geodaetica et Geophysica*, *57*(1), 107–127. https://doi.org/10.1007/s40328-021-00368-y

Mannucci, A. J., Iijima, B., Sparks, L., Pi, X., Wilson, B., & Lindqwister, U. (1999). Assessment of global TEC mapping using a three-dimensional electron density model. *Journal of Atmospheric and Solar-Terrestrial Physics*, *61*(16), 1227–1236. https://doi.org/10.1016/S1364-6826(99)00053-X

Mannucci, A. J., Wilson, B. D., Yuan, D. N., Ho, C. H., Lindqwister, U. J., & Runge, T. F. (1998). A global mapping technique for GPS-derived ionospheric total electron content measurements. *Radio Science*, *33*(3), 565–582. https://doi.org/10.1029/97rs02707

Martire, L., Runge, T. F., Meng, X., Krishnamoorthy, S., Vergados, P., Mannucci, A. J., et al. (2024). The JPL-GIM algorithm and products: Multi-GNSS high-rate global mapping of total electron content. *Journal of Geodesy*, *98*(5), 44. https://doi.org/10.1007/s00190-024-01860-3

Maruyama, N., Sun, Y.-Y., Richards, P. G., Middlecoff, J., Fang, V., Fuller-Rowell, T. J., et al. (2016). A new source of the midlatitude ionospheric peak density structure revealed by a new Ionosphere-Plasmasphere model. *Geophysical Research Letters*, *43*(6), 2429–2435. https://doi.org/10.1002/2015GL067312

Maruyama, T., Hozumi, K., Ma, G., Supnithi, P., Tongkasem, N., & Wan, Q. (2021). Double-thin-shell approach to deriving total electron content from GNSS signals and implications for ionospheric dynamics near the magnetic equator. *Earth Planets and Space*, *73*(1), 109. https://doi.org/10.1186/s40623-021-01427-y

Matzka, J., Stolle, C., Yamazaki, Y., Bronkalla, O., & Morschhauser, A. (2021). The geomagnetic Kp index and derived indices of geomagnetic activity. *Space Weather*, *19*(5), e2020SW002641. https://doi.org/10.1029/2020SW002641

McClure, J. P., Hanson, W. B., & Hoffman, J. H. (1977). Plasma bubbles and irregularities in the equatorial ionosphere. *Journal of Geophysical Research*, *82*(19), 2650–2656. https://doi.org/10.1029/JA082i019p02650

Mendillo, M., Huang, C.-L., Pi, X., Rishbeth, H., & Meier, R. (2005). The global ionospheric asymmetry in total electron content. *Journal of Atmospheric and Solar-Terrestrial Physics*, *67*(15), 1377–1387. https://doi.org/10.1016/j.jastp.2005.06.021

Meng, X., & Verkhoglyadova, O. P. (2023). Total electron content intensification dataset for years 2003 to 2022 [Dataset]. *JPL Open Repository*. https://doi.org/10.48577/jpl.KXY5BW

Meng, X., Verkhoglyadova, O. P., Chapman, S. C., Watkins, N. W., & Cafolla, M. (2024). Statistical characteristics of total electron content intensifications on global ionospheric maps. *Space Weather*, *22*(1), e2023SW003695. https://doi.org/10.1029/2023SW003695

Niehof, J. T., Morley, S. K., Welling, D. T., & Larsen, B. A. (2022). The SpacePy space science package at 12 years. *Frontiers in Astronomy and Space Sciences*, *9*. https://doi.org/10.3389/fspas.2022.1023612

Nigussie, M., Jakowski, N., & Hoque, M. (2022). Characterization and climatological modeling of Equatorial Ionization Anomaly (EIA) crest position. *Journal of Geophysical Research: Space Physics*, *127*(12), 2022JA030798. https://doi.org/10.1029/2022JA030798

Nikitina, L., Fiori, R. A. D., Ghoddousi-Fard, R., & Waddington, G. H. (2022). Statistical analysis of large and extreme global ionospheric total electron content. *Journal of Atmospheric and Solar-Terrestrial Physics*, *229*, 105841. https://doi.org/10.1016/j.jastp.2022.105841

Oryema, B., Jurua, E., D'ujanga, F. M., & Ssebiyonga, N. (2015). Investigation of TEC variations over the magnetic equatorial and equatorial anomaly regions of the African sector. *Advances in Space Research*, *56*(9), 1939–1950. https://doi.org/10.1016/j.asr.2015.05.037

Palacios, J., Guerrero, A., Cid, C., Saiz, E., & Cerrato, Y. (2017). Defining scale thresholds for geomagnetic storms through statistics. *Natural Hazards and Earth System Sciences Discussions*. https://doi.org/10.5194/nhess-2017-367

Patil, A. S., Nade, D. P., Taori, A., Pawar, R. P., Pawar, S. M., Nikte, S. S., et al. (2023). A brief review of equatorial plasma bubbles. *Space Science Reviews*, *219*(1), 16. https://doi.org/10.1007/s11214-023-00958-y

Pedregosa, F., Varoquaux, G., Gramfort, A., Michel, V., Thirion, B., Grisel, O., et al. (2011). Scikit-learn: Machine learning in Python. *Journal of Machine Learning Research*, *12*, 2825–2830.

Poduval, B., McPherron, R. L., Walker, R., Himes, M. D., Pitman, K. M., Azari, A. R., et al. (2023). AI-ready data in solar physics and space science: Concerns, mitigation and recommendations. *Frontiers in Astronomy and Space Sciences*, *10*. https://doi.org/10.3389/fspas.2023.1203598

Pulkkinen, T. (2007). Space weather: Terrestrial perspective. *Living Reviews in Solar Physics*, *4*, 1. https://doi.org/10.12942/lrsp-2007-1

Qian, L., Burns, A. G., Solomon, S. C., & Wang, W. (2013). Annual/semiannual variation of the ionosphere. *Geophysical Research Letters*, *40*(10), 1928–1933. https://doi.org/10.1002/grl.50448

Roma-Dollase, D., Hernández-Pajares, M., Krankowski, A., Kotulak, K., Ghoddousi-Fard, R., Yuan, Y., et al. (2018). Consistency of seven different GNSS global ionospheric mapping techniques during one solar cycle. *Journal of Geodesy*, *92*(6), 691–706. https://doi.org/10.1007/s00190-017-1088-9

Rukundo, W., Shiokawa, K., Elsaid, A., AbuElezz, O. A., & Mahrous, A. M. (2023). A machine learning approach for total electron content (TEC) prediction over the northern anomaly crest region in Egypt. *Advances in Space Research*, *72*(3), 790–804. https://doi.org/10.1016/j.asr.2022.10.052

Russell, C. T., & McPherron, R. L. (1973). Semiannual variation of geomagnetic activity. *Journal of Geophysical Research*, *78*(1), 92–108. https://doi.org/10.1029/JA078i001p00092

Seemala, G. K., & Valladares, C. E. (2011). Statistics of total electron content depletions observed over the South American continent for the year 2008. *Radio Science*, *46*(5), RS5019. https://doi.org/10.1029/2011RS004722

Sparks, L., Altshuler, E., Pandya, N., Blanch, J., & Walter, T. (2021). WAAS and the ionosphere—A historical perspective: Monitoring storms. *Navigation*, *69*(1), navi503. https://doi.org/10.33012/navi.503

Takahashi, H., Wrasse, C. M., Denardini, C. M., Pádua, M. B., de Paula, E. R., Costa, S. M. A., et al. (2016). Ionospheric TEC weather map over South America. *Space Weather*, *14*(11), 937–949. https://doi.org/10.1002/2016SW001474

Tsai, T. C., Jhuang, H. K., Lee, L. C., & Ho, Y. Y. (2019). Ionospheric peaked structures and their local time, seasonal, and solar activity dependence based on Global Ionosphere Maps. *Journal of Geophysical Research: Space Physics*, *124*(10), 7994–8014. https://doi.org/10.1029/2019JA026899

Tulasi Ram, S., Su, S.-Y., & Liu, C. H. (2009). FORMOSAT-3/COSMIC observations of seasonal and longitudinal variations of equatorial ionization anomaly and its interhemispheric asymmetry during the solar minimum period. *Journal of Geophysical Research*, *114*(A6), A06311. https://doi.org/10.1029/2008JA013880

Vaishnav, R., Jacobi, C., & Berdermann, J. (2019). Long-term trends in the ionospheric response to solar extreme-ultraviolet variations. *Annales Geophysicae*, *37*(6), 1141–1159. https://doi.org/10.5194/angeo-37-1141-2019

Verkhoglyadova, O., Maus, N., & Meng, X. (2021). Classification of high density regions in Global Ionospheric Maps with neural networks. *Earth and Space Science*, *8*(7), e2021EA001639. https://doi.org/10.1029/2021EA001639

Verkhoglyadova, O., Meng, X., & Kosberg, J. (2022). Understanding large-scale structure in global ionospheric maps with visual and statistical analyses. *Frontiers in Astronomy and Space Sciences*, *9*, 852222. https://doi.org/10.3389/fspas.2022.852222

Virtanen, P., Gommers, R., Oliphant, T. E., Haberland, M., Reddy, T., Cournapeau, D., et al. (2020). SciPy 1.0: Fundamental algorithms for scientific computing in Python. *Nature Methods*, *17*(3), 261–272. https://doi.org/10.1038/s41592-019-0686-2

Walker, G. O. (1981). Longitudinal structure of the F-region equatorial anomaly—A review. *Journal of Atmospheric and Terrestrial Physics*, *43*(8), 763–774. https://doi.org/10.1016/0021-9169(81)90052-0

Wang, X.-L., Wan, Q.-T., Ma, G.-Y., Li, J.-H., & Fan, J.-T. (2016). *The influence of ionospheric thin shell height on TEC retrieval from GPS* (Vol. 16). National Astronomical Observatories of Chinese Academy of Sciences and IOP Publishing. Number 7, 16. https://doi.org/10.1088/1674-4527/16/7/116

Wanliss, J. A., & Showalter, K. M. (2006). High-resolution global storm index: Dst versus SYM-H. *Journal of Geophysical Research*, *111*(A2), A02202. https://doi.org/10.1029/2005JA011034

Welch, P. (1967). The use of fast Fourier transform for the estimation of power spectra: A method based on time averaging over short, modified periodograms. *IEEE Transactions on Audio and Electroacoustics*, *15*(2), 70–73. https://doi.org/10.1109/TAU.1967.1161901

Wood, A. G., Alfonsi, L., Clausen, L. B. N., Jin, Y., Spogli, L., Urbář, J., et al. (2022). Variability of ionospheric plasma: Results from the ESA Swarm mission. *Space Science Reviews*, *218*(6), 52. https://doi.org/10.1007/s11214-022-00916-0

Xiong, B., Wang, Y., Li, X., Li, Y., & Yu, Y. (2022). Constructing a global ionospheric TEC map with a high spatial and temporal resolution by spherical harmonic functions. *Astrophysics and Space Science*, *367*(9), 85. https://doi.org/10.1007/s10509-022-04120-y

Yasyukevich, A. S., & Yasyukevich, Y. V. (2021). Diurnal, seasonal and solar-cycle variations in the short-term variability of total electron content at mid latitudes. In *Proceedings of URSI GASS Conference 2021, Rome, Italy*. Retrieved from https://www.ursi.org/proceedings/procGA21/papers/URSIGASS2021-Th-G10-AM1-3.pdf

Yaya, P., Hecker, L., Dudok de Wit, T., Fèvre, C. L., & Bruinsma, S. (2017). Solar radio proxies for improved satellite orbit prediction. *Journal of Space Weather and Space Climate*, *7*, A35. https://doi.org/10.1051/swsc/2017032

Yue, X., Schreiner, W. S., Kuo, Y.-H., & Lei, J. (2015). Ionosphere equatorial ionization anomaly observed by GPS radio occultations during 2006–2014. *Journal of Atmospheric and Solar-Terrestrial Physics*, *129*, 30–40. https://doi.org/10.1016/j.jastp.2015.04.004

Zhang, Q., & Zhao, Q. (2019). Analysis of the data processing strategies of spherical harmonic expansion model on global ionosphere mapping for moderate solar activity. *Advances in Space Research*, *63*(3), 1214–1226. https://doi.org/10.1016/j.asr.2018.10.031